Supporting Information

Metal-free Platforms for Molecular Thin Films as High-performance Supercapacitors

Ritu Gupta[a], Ankur Malik[a], Kusum Kumari[b], Saurabh Kumar Singh[b], Vincent Vivier*[c] and Prakash Chandra Mondal*[a]

[a]Department of Chemistry, Indian Institute of Technology Kanpur, Uttar Pradesh 208016, India

[b]Department of Chemistry, Indian Institute of Technology Hyderabad, Telangana 502285, India

[c]Sorbonne Université, CNRS, Laboratoire de Réactivité de Surface, 4 place Jussieu, Paris 75005 Cedex 05, France

E-mail: vincent.vivier@sorbonne-universite.fr (VV); pcmondal@iitk.ac.in (PCM)

Contents

1. Materials and Instrumentations:

1a. Materials. 1-aminoanthracene (90%), 1-aminopyrene (97%), 1-aminonaphthalene (97%), sodium nitrite (97%), tertiary butyl nitrite (90%), tetrafluoroboric acid (HBF_4, 48% in water), tetrabutylammonium perchlorate (TBAP, 98%) were purchased from Sigma-Aldrich (Bangalore, India). All these chemicals, including hydrochloric acid (Finar Chemicals), sulphuric acid (Finar Chemicals), and acetonitrile (Avantore, HPLC-grade), were used as received. Cylindrical graphite rods (GR, 3 mm × 305 mm) used for electrochemical grafting were purchased from SPI supplies. Eveready dry cells were used to isolate graphite rods, cleaned with acetone for 40 minutes, and then with distilled water. Single-side ITO-coated glass substrates (sheet resistance <10 Ω/sq, thickness 1.1 mm, and transmittance >83% in the visible regime) were purchased from Nanoshel UK Ltd. Diazonium salts of all three amino precursors were synesized as discussed later.

1b. Instrumentations. FT-IR spectra were recorded in an attenuated total reflectance (ATR) mode by Bruker ALPHA II FT-IR spectrometer (software: OPUS) within a spectral range of $4000 - 500$ cm^{-1} (signal-to-noise ratio of 55,000:1) having a high humidity optics by ZnSe beamsplitter and ZnSe windows. JASCO V-770 UV-Visible-NIR spectrophotometer (light source: tungsten-deuterium lamp) was employed to record UV-vis spectra from $\lambda = 200$ to 800 nm in a double beam mode using a 10 mm optical path length of quartz cuvettes with a 400 nm min^{-1} scan. Before measurement, cuvettes were cleaned with isopropanol and acetonitrile and dried properly. For thickness measurement, D-ANT was electrochemically grafted on ITO substrates using similar grafting parameters. In tapping mode, surface morphology was analyzed via atomic force microscopy (AFM) using Asylum Research (Oxford Instruments) with a silicon probe having a force constant of 0.5 N/m. The images were recorded at 0.60 Hz, set point in the range of 760 mV-730 mV with a drive frequency of 65.38 kHz. The thickness was evaluated by scratching the film with a sharp needle, and a line profile was drawn to get the thickness. For thin film characterization on GR, thin film X-ray diffraction (XRD) was performed on bare GR and modified GR at room temperature in the 2θ range of 5° to 90° with PANalytical Empyrean ACMS 101 at 2° min^{-1} scan rate. The surface morphology of the bare GR and electrochemically modified GR were analyzed by field emission scanning electron microscopy (FE-SEM) employing Zeiss, model: supra40VP. Further, Raman spectra were recorded using SP2500i Acton instruments for monochromator and Spectrograph, the laser source 532 nm from laser quantum. X-ray photoelectron spectroscopy (XPS) was performed with Auger Electron Spectroscopy (AES) module PHI 5000 Versa Prob II, with a monochromator Al K-α source (1486.6 eV), hemispherical analyzer, and multichannel detector. Survey spectra of individual samples were obtained, followed by high-resolution spectra of C1s and N1s. Static water contact angle measurement was performed with a Kruss DSA25 goniometer. ~ 2 μL droplet of water was dropped on bare GR and modified GR, and a high-resolution camera (1.5X) was utilized to capture the high-resolution image. N_2 adsorption-desorption

measurement based on the Brunauer-Emmett-Teller (BET) principle was performed using Autosorb I; Quatachrome Corp. Desorption temperature for all the substrates was kept the same at 90°C. All electrochemical characterization was performed using a three-electrode system in 1 M H_2SO_4 that was purged with nitrogen for 15 min prior to all measurements employing a Metrohm Autolab Potentiostat (Model: 204, software nova-2.14). GR and modified GR were used as working electrodes, and a platinum wire was employed as a counter electrode. We used an $Ag/AgNO_3$ (10 mM $AgNO_3$ in acetonitrile with 0.1 M TBAP supporting electrolyte) reference electrode for a non-aqueous solvent, whereas an Ag/AgCl (saturated KCl) electrode was used for an aqueous solvent. Before and after measurements, reference electrodes were properly cleaned with their respective solvents, and the counter electrode was cleaned with distilled water. For constant current charge/discharge measurements, bare GR and modified GR substrates were charged from $-$ 0.1 V vs. Ag/AgCl to $+$ 0.7 V vs. Ag/AgCl and discharged from $+$ 0.7 V vs. Ag/AgCl to $-$ 0.1 V vs. Ag/AgCl at different applied current densities. Solid-state I-V measurements were performed using a KEITHLEY 2604B source meter via two-probes contact.

2. Synthesis and characterizations of diazonium salts

2a. Synthesis of anthracene, pyrene, and naphthalene diazonium salts

To synthesize anthracene diazonium salt (**Scheme S1a**), 1 mmol of 1-amino anthracene was dissolved in ethanol in a round-bottomed flask. The solution was cooled down to 0°C in a NaCl-added ice bath. Cold tertiary butyl nitrite (0.6 mmol) was added dropwise into the precursor solution and stirred at 0°C for 30 minutes. To replace the counter ion, HBF_4 (~ 2 mL) was added into the solution in a drop-wise manner. The solid precipitate was vacuum filtered, washed with cold diethyl ether thrice, and stored at $-$ 5°C (**Scheme S1**).
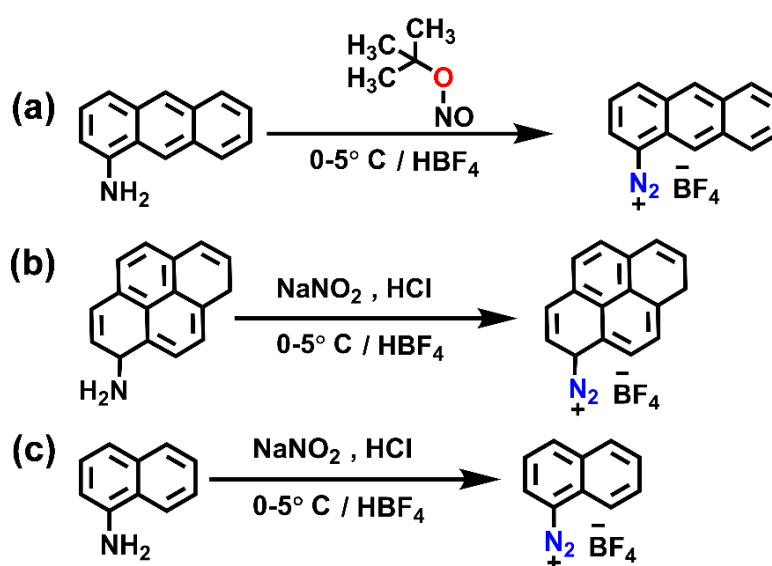
Scheme S1. Synthesis scheme for the preparation of (a) anthracene, (b) pyrene, and (c) naphthalene diazonium tetrafluoroborate.

To synthesize diazonium salts of pyrene and naphthalene, 1 mmol of their individual amine precursor was added into a round-bottomed flask, and concentrated HCl (1-2 mL) was added to the amine precursor. The solution was cooled down to 0°C in a NaCl-added ice bath. Cold sodium nitrite (1 mmol) was added dropwise into the precursor solution and stirred at 0°C for 30 minutes. To replace the counter ion, HBF$_4$ (~ 2 mL) was added into the solution in a drop-wise manner. The solid precipitate was vacuum filtered and washed with cold diethyl ether three times and stored at $-$ 5°C (**Scheme S1b & S1c**).

2b. Characterization of synthesized diazonium salts

Freshly prepared diazonium salts were characterized by FT-IR and UV-vis spectroscopy techniques. **Fig S1a** shows the FT-IR spectra of amino anthracene (A-ANT) and diazonium anthracene tetrafluoroborate, wherein a sharp peak at ~2229 cm^{-1} confirms the presence of diazonium group (-N$_2^+$). A peak at ~1624 cm^{-1} was observed, which was assigned to the carbon double bond present in anthracene moiety. Along with this, a sharp peak at 1041 cm^{-1} was observed, which indicates the presence of B-F stretching from tetrafluoroborate counter ion. The synthesized D-ANT salt was characterized by UV-visible spectroscopy, as shown in **Fig S1(b)**. A redshift of maximum absorbance by 37 nm and loss of absorption peak at 395 nm (n→π* transition) in D-ANT confirms the formation of diazonium anthracene salt. Similarly, the pyrene and naphthalene diazonium tetrafluoroborate were characterized by FT-IR and UV-visible spectroscopy. A sharp peak at ~2213 cm^{-1} in D-PYR and at ~2252 cm^{-1} in D-NAPH confirms the formation of diazonium and loss of (n→π* transition) at 362 nm in D-PYR and 332 nm in D-NAPH in UV-visible spectra further confirms the formation of diazonium in both the compounds (**Fig S2-S3**).
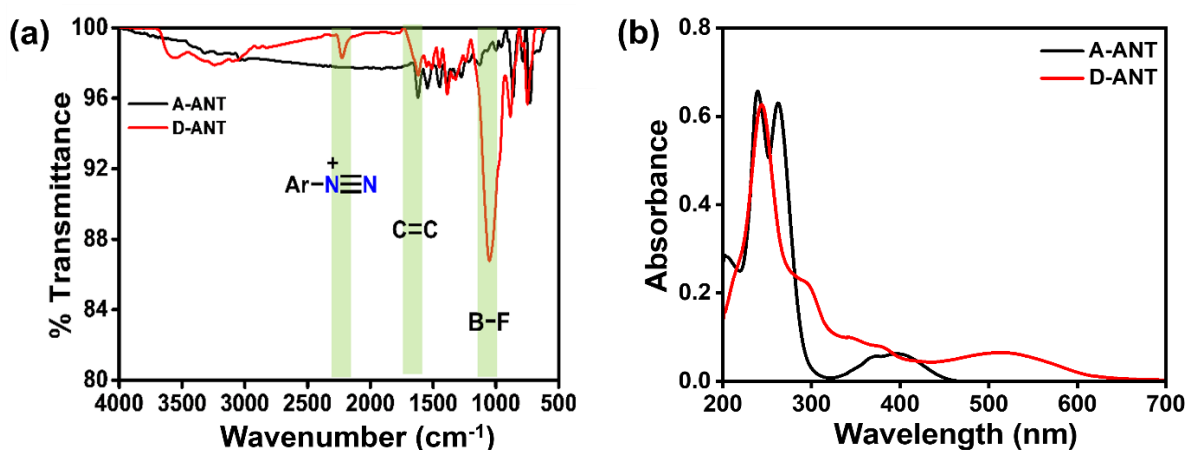

Fig S1. Comparison of (a) FT-IR spectra of A-ANT and D-ANT, characteristic stretching frequencies are highlighted, and (b) UV-visible spectra of A-ANT and D-ANT, y-axis (absorbance) of D-ANT is multiplied by 2.
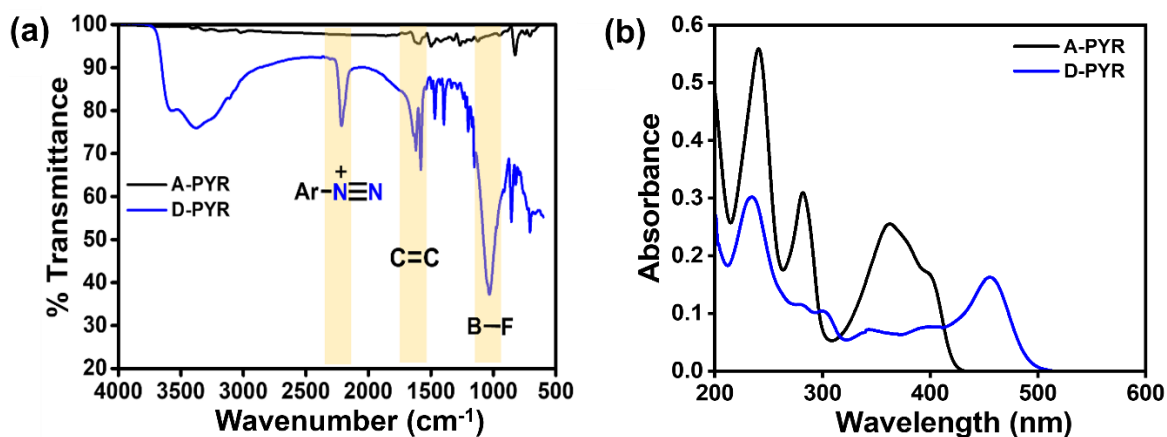
Fig S2. Comparison of (a) FT-IR spectra of A-PYR and D-PYR, characteristic stretching frequencies are highlighted, and (b) UV-visible spectra of A-PYR and D-PYR, y-axis (absorbance) of D-PYR was multiplied by 3.
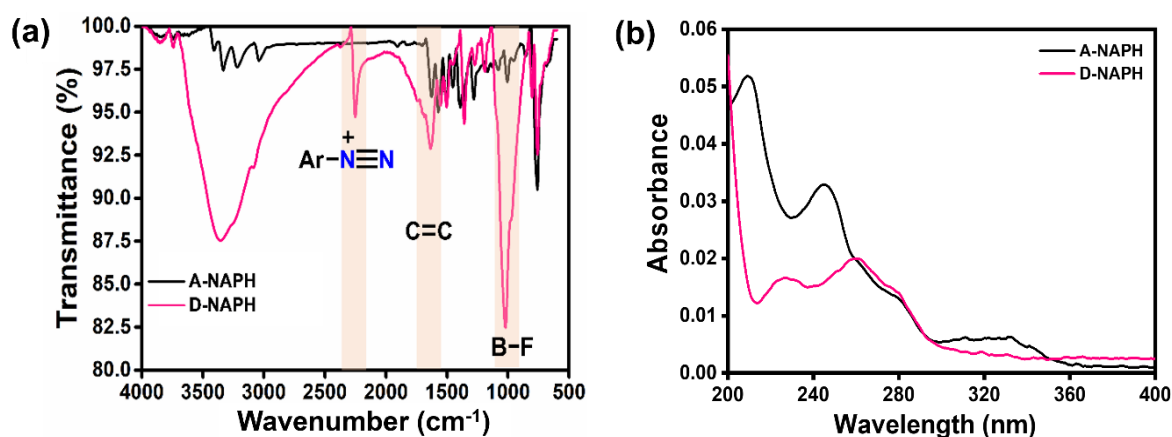

Fig S3. Comparison of (a) FT-IR spectra of A-NAPH and D-NAPH, characteristic stretching frequencies are highlighted, and (b) UV-visible spectra of A-NAPH and D-NAPH.

3. Electrochemical grafting of diazonium salts on graphite rod (GR)

Before electrochemical grafting, the graphite rod (GR) was pretreated with distilled water for 15 min and then dried with a nitrogen gun. The GRs were dried in an oven at 100°C for 10 min to remove any traces of water present and then cleaned by a nitrogen gun to remove unwanted contaminants. E-Chem grafting was performed employing a conventional three-electrode system. GR was used as a working electrode, and Ag/AgNO$_3$ and Pt were used as reference and counter electrodes. All electrochemical measurements were recorded at room temperature. For electrochemical grafting, concentrations of all diazonium solutions were kept the same, that is, 5 mM in HPLC-grade acetonitrile (ACN) with 0.1 M tetrabutylammonium perchlorate (TBAP) as a supporting electrolyte. Prior to E-Chem grafting, all diazonium solutions were deoxygenated by nitrogen purging for 15-20 min. After modification, the GR substrates were heavily rinsed with ACN to remove any physiosorbed materials.
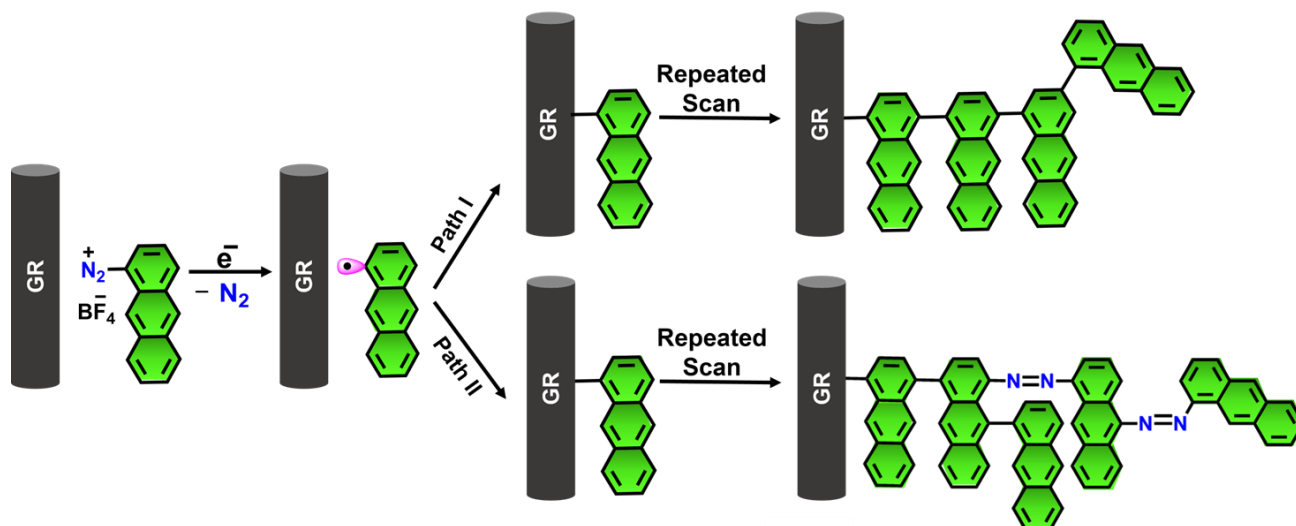
Fig S4. Schematic description of proposed E-Chem grafting of D-ANT on GR electrode.
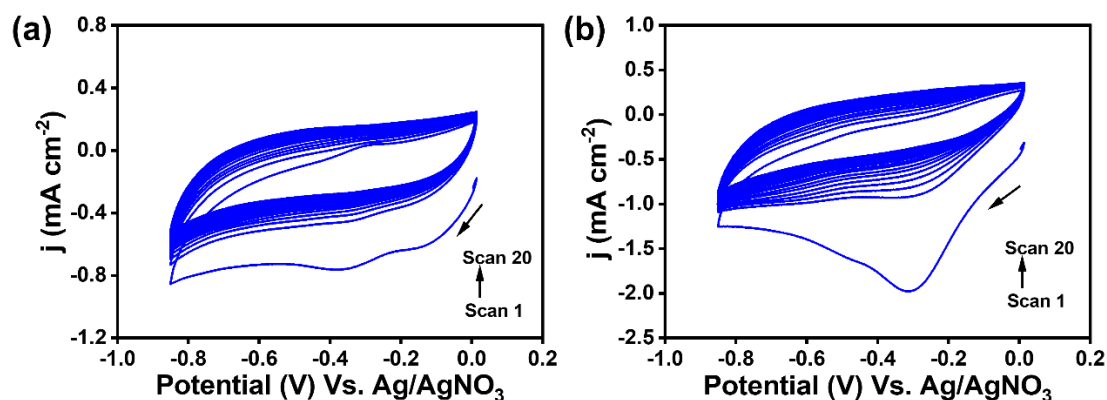

Fig S5. (a) Cyclic voltammograms of E-Chem grafting of (a) pyrene (PYR), and (b) naphthalene (NAPH) diazonium salts of 5 mM concentration on graphite rod using 0.1 M TBAP as supporting electrolyte at 100 mV s^{-1} up to 20 scans.

Electrochemical parameters and surface coverage are given in **Table S1**. Surface coverage was calculated using a standard procedure (see Eq. (i)) Where i_p is peak current, F is Faraday constant, υ is scan rate, *A* is the effective area of the electrode, Γ^* is surface coverage of adsorbed species in mol cm^{-2}.

$$i_p = \frac{n^2 \, F^2}{4 \, R \, T} \times \upsilon \, A \, \Gamma^* \qquad \text{(i)}$$

Table S1. Electrochemical grafting parameters of ANT, PYR, and NAPH diazonium on GR electrode.

Serial No.	Sample	Concentration of diazonium (mM)	Potential window (V)	Scan rate (mV s⁻¹)	scan	Surface Coverage (mol cm⁻²)
1.	ANT/GR	5	$(+0.01) - (-0.85)$	100	20	$5.0 \pm 0.64 \times 10^{-12}$
2.	PYR/GR	5	$(+0.01) - (-0.85)$	100	20	$9.4 \pm 0.22 \times 10^{-13}$
3.	NAPH/GR	5	$(+0.01) - (-0.85)$	100	20	$6.6 \pm 0.45 \times 10^{-13}$

4. Atomic force microscopy measurements to determine molecular thickness

To determine the thickness of ANT layers, D-ANT was E-Chem grafted on an indium tin oxide (ITO) substrate with the same electrochemical parameters used for GR modification.
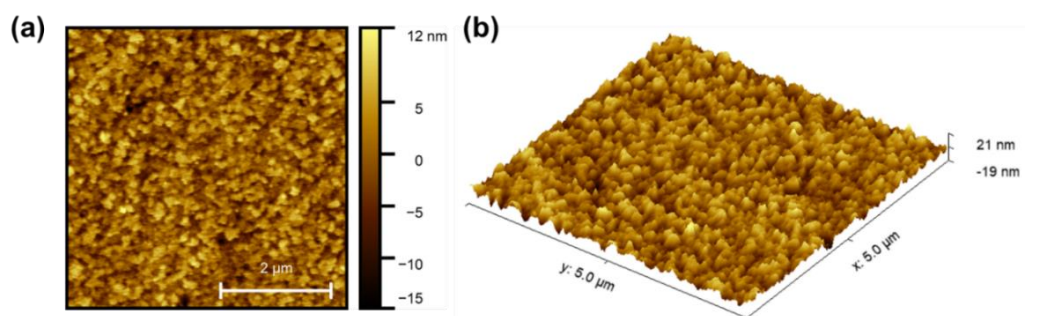

Fig S6. (a) Tapping mode two-dimensional AFM image of ANT film (5×5 µm²) region, and (b) Three-dimensional image for the same.

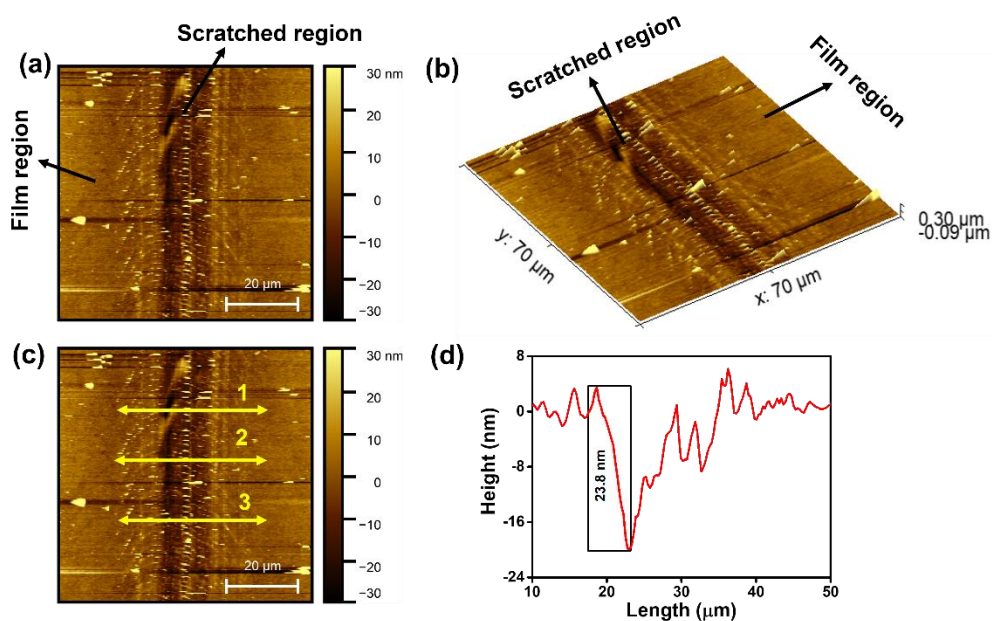**Fig S7.** (a) Tapping mode two-dimensional AFM image of ANT film and scratched film region in 70×70 µm² region, (b) three-dimensional image for the same, and (c,d) Line profile diagram of the ANT film after scratching with a sharp needle.

5. UV-vis absorption spectra of anthracene, pyrene, and naphthalene oligomeric films recorded on ITO-coated glass substrates.
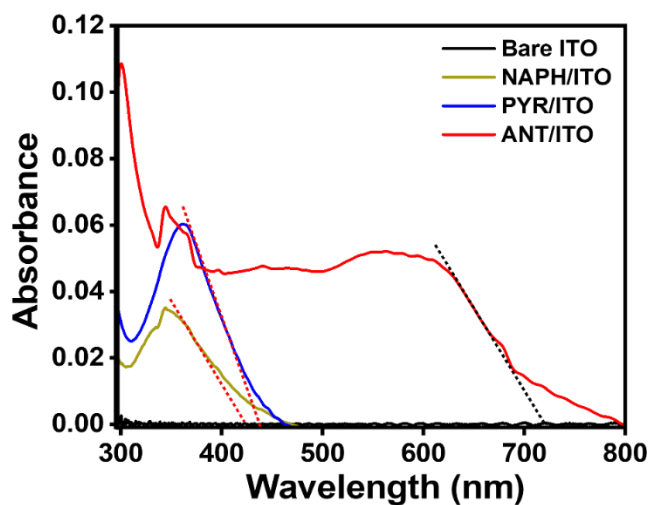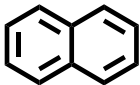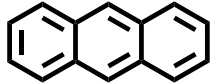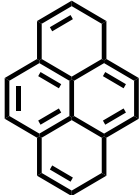

Fig S8. Comparison of UV-vis spectra of ITO baseline corrected NAPH, PYR, and ANT thin films grafted on ITO. These data were employed to determine the optical band gaps.

Table S2. Optical band gap of thin film grafted on ITO substrate estimated from UV-vis spectrum.

S. No.	Sample	Band gap (eV)
1.	ANT/ITO	1.72
2.	PYR/ITO	2.8
3.	NAPH/ITO	2.9

Table S3. Band gap energy of a single molecule of naphthalene, anthracene, and pyrene obtained from literature.

Single Molecule	Band gap (eV)	Ref.
	4.3	[1]
	3.2	[1]
	3.4	[1]

6. X-ray diffraction (XRD) pattern of bare GR, ANT/GR, PYR/GR, and NAPH/GR electrode
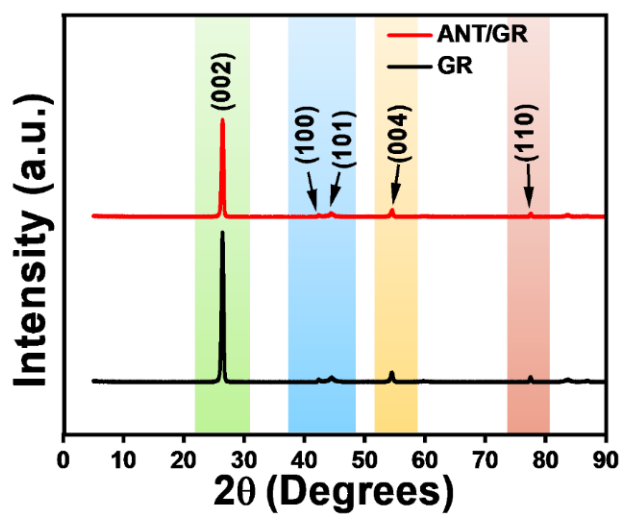
Fig S9. Comparison of X-ray diffraction (XRD) pattern of ANT grafted thin films on GR electrode, and bare GR.
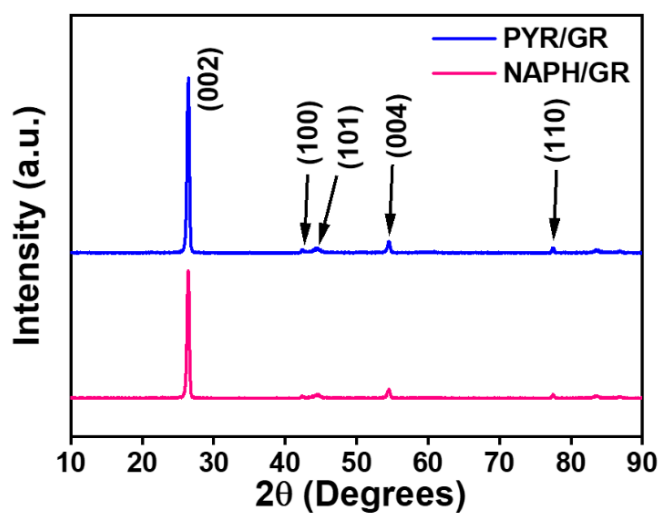
Fig S10. Comparison of X-ray diffraction (XRD) pattern of NAPH (magenta), and PYR (blue) grafted thin films on GR electrode.
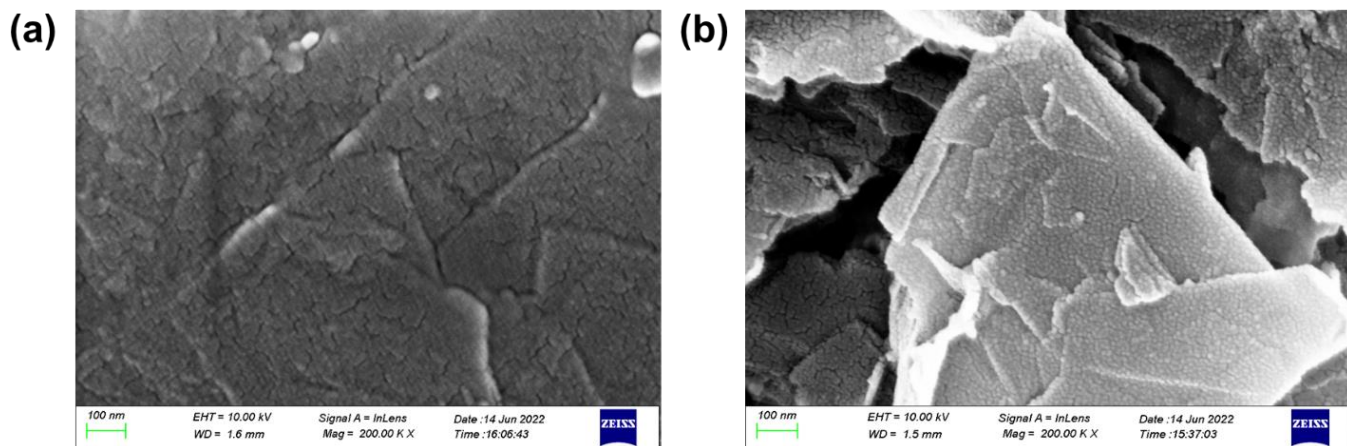
Fig S11. FE-SEM image of (a) bare GR electrode, and (b) ANT/GR electrode.
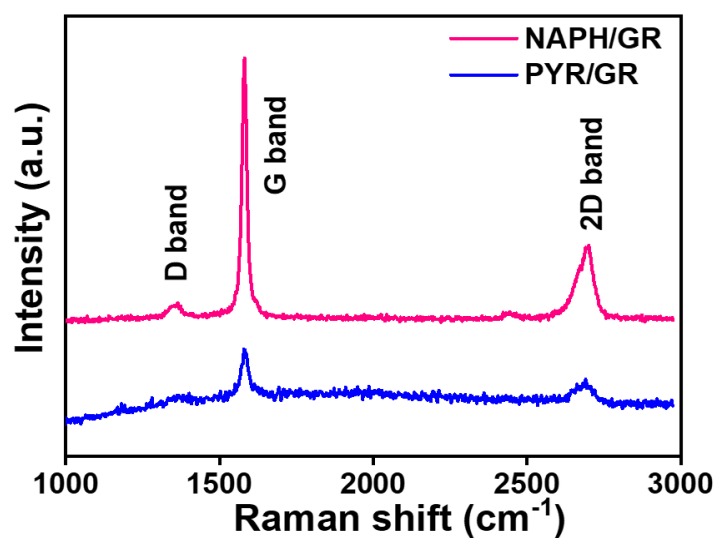
Fig S12. Comparison of Raman spectra of NAPH/GR, and PYR/GR.

7. X-ray photoelectron spectroscopy (XPS) measurements of bare GR and ANT/GR
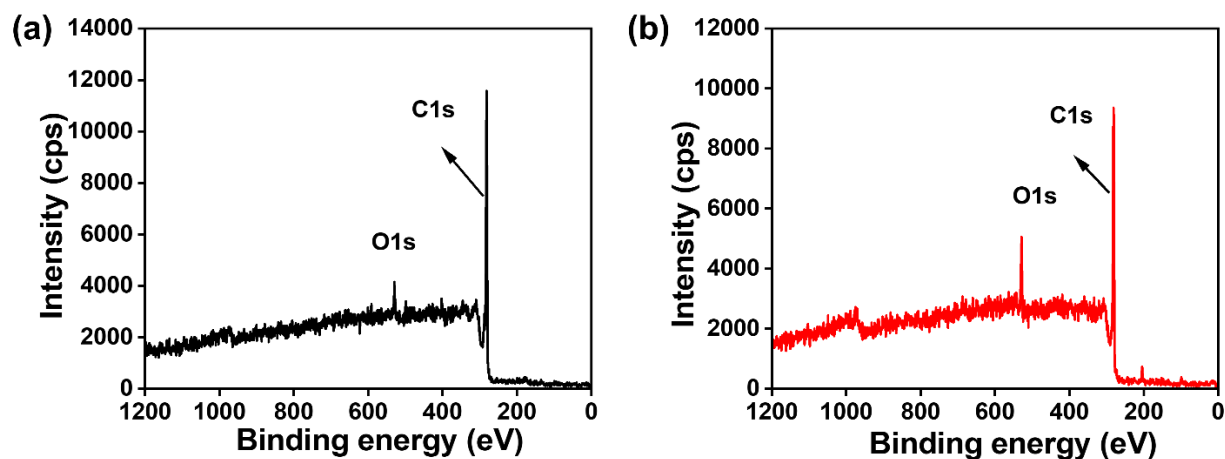
Fig S13. Overall XPS survey spectra of (a) bare GR, and (b) ANT/GR. The characteristic signals are highlighted.
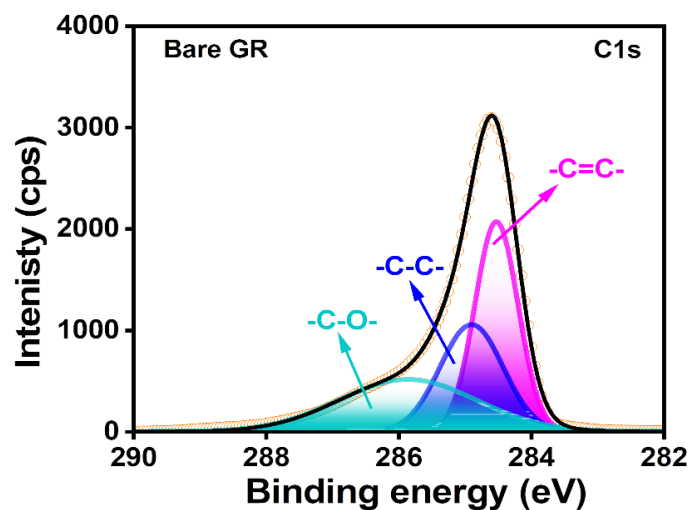
Fig S14. Deconvulated XPS spectra of C1s of bare GR. The characteristic signals are highlighted.
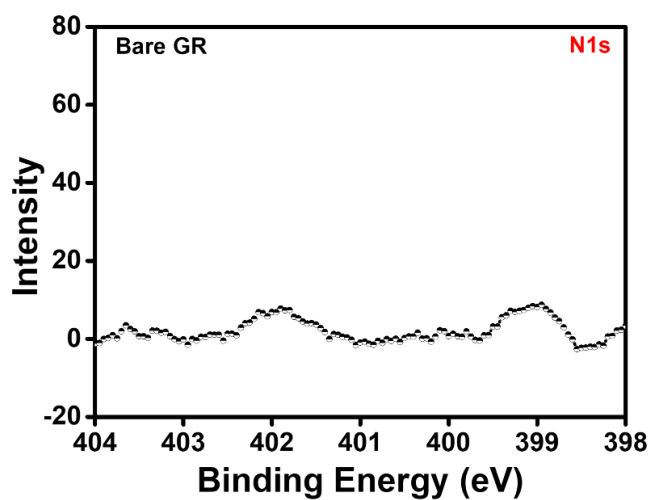
Fig S15. XPS spectra of N1s of bare GR.

Table S4. XPS peak binding energy of elements in bare GR and ANT/GR

| S.N.	Electrode	Element	State/term	Binding energy (eV)
1	Bare GR	C	1s	284.52
				285.90
				285.86
2.	ANT/GR	C	1s	284.45
				284.78
				285.49
				286.10
		N	1s	399.53
				400.45
				402.22
				402.77

8. Static water contact angle analysis of bare GR, ANT/GR, PYR/GR, and NAPH/GR electrode

(a) Bare GR
Left CA = 129.2°
Right CA = 129.4°
"HYDROPHOBIC"

(b) ANT/GR
Left CA = 61.2°
Right CA = 62.0°
"HYDROPHILIC"

(c) NAPH/GR
Left CA = 64.3°
Right CA = 60.7°
"HYDROPHILIC"

(d) PYR/GR
Left CA = 74.2°
Right CA = 73.7°
"HYDROPHILIC"
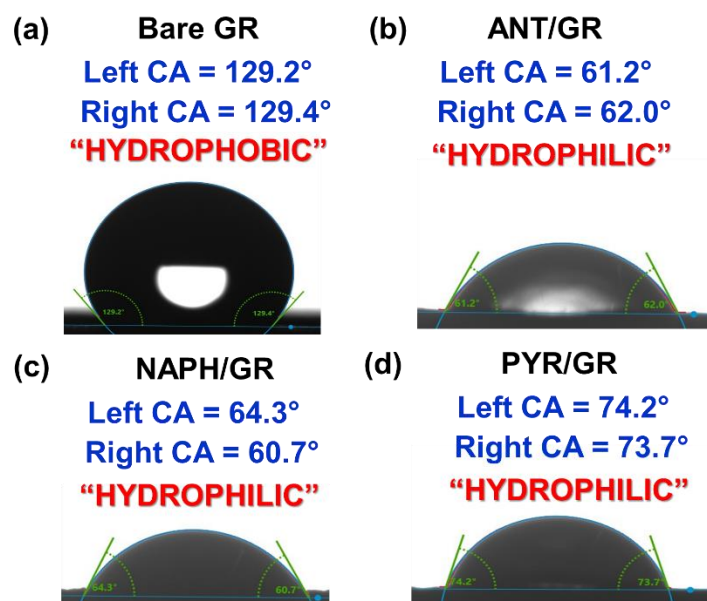
Fig S16. Static water contact angle of (a-d) bare GR, ANT/GR, NAPH/GR, and PYR/GR.

Table S5. Static water contact angle measurement of bare GR, ANT/GR, NAPH/GR, and PYR/GR at different places

Sample	Place 1		Place 2		Place 3		AVG. CA
	Left contact angle	Right contact angle	Left contact angle	Right contact angle	Left contact angle	Right contact angle	
Bare GR	129.2°	129.4°	128.9°	128.7°	123.5°	123.6°	127° ± 0.02°
ANT/GR	65.9°	60.2°	63.2°	69.6°	61.2°	62.0°	63.5° ± 0.77°
NAPH/GR	57.2°	62.4°	64.3°	60.7°	54.4°	57.4°	59.4° ± 1.1°
PYR/GR	77.7°	74.7°	74.2°	73.7°	70.1°	70.1°	73.4° ± 0.82°

9. BET surface area analysis of bare and ANT-modified GR

Fig S17. Nitrogen adsorption-desorption isotherm of (a) bare GR, and (b) ANT/GR.

Fig S18. Pore size distribution of (a) bare GR, and (b) ANT/GR.

10. Computational methodology

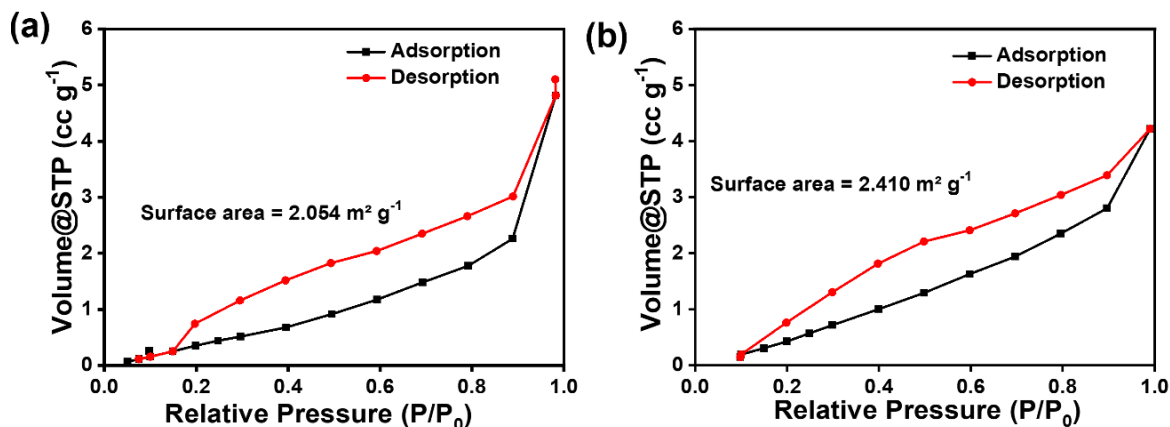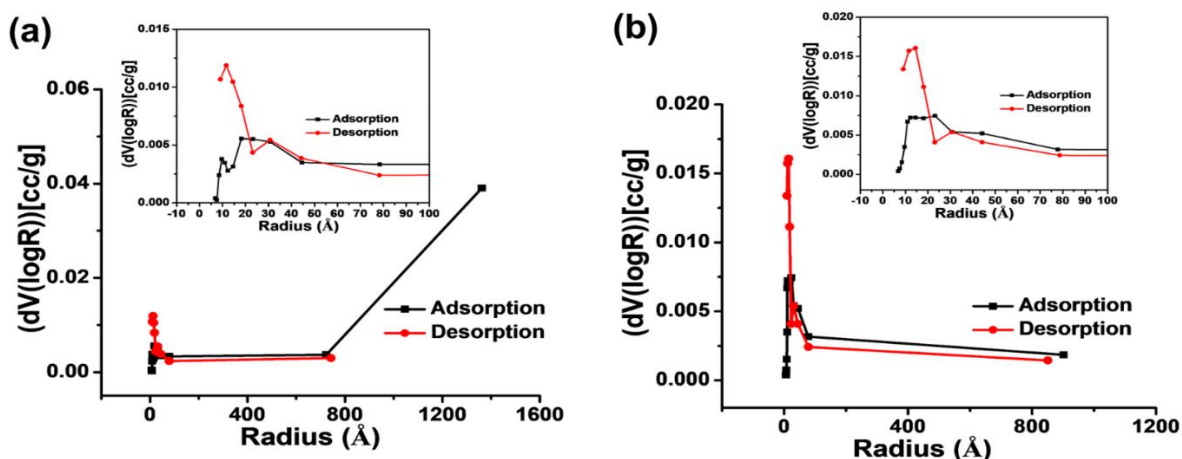To simulate the target system computationally, we optimized a two-dimensional monolayer of graphene arranged in a hexagonal lattice structure with specific lattice parameters: a=b= 19.680Å, c = 33.600 Å, and α = 120°, along with a carbon-carbon distance of 1.43 Å. On this supercell, one molecule was chemisorbed on the graphene layer, and a vacuum region of 20 Å was introduced in the third dimension (z-axis) to avoid spurious electrostatic interactions between the replicas. We conducted periodic density functional theory (DFT) calculations using the VASP code,[2,3] employing an 8x8 supercell containing 128 carbon atoms. All the optimizations were done at the gamma point. The wave functions within the supercell were expanded using a plane-wave basis set, with an energy cutoff set at 520 eV. Electronic cores were treated using the projector-augmented wave method.[4,5] Convergence criteria were established for energy (10^{-6} eV per unit cell) and atomic force (0.05 eV per Å). Additionally, we incorporated Grimme's Method D3 for dispersion correction with Becke-Johnson damping. To ensure electronic convergence, a Gaussian broadening of 0.2 eV was applied using the smearing technique.
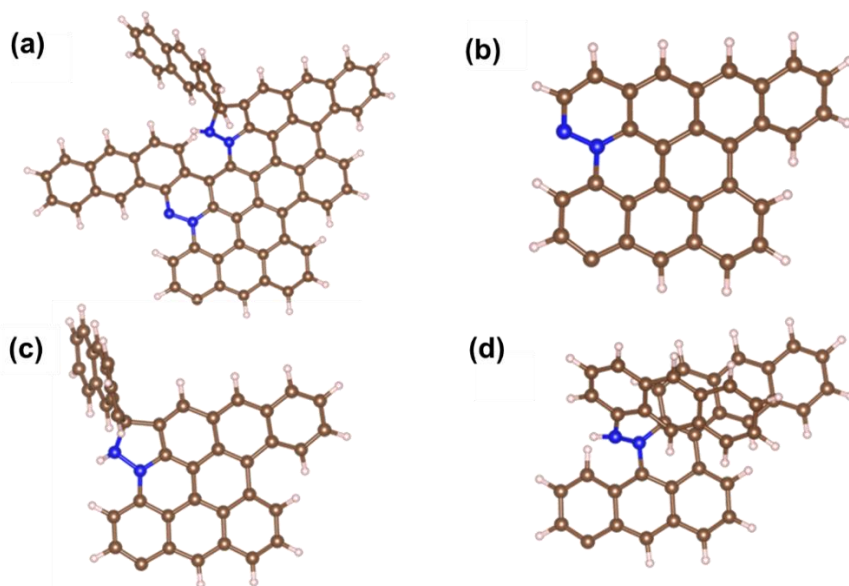
Fig S19. DFT optimized four possible structures of anthracene with different Nitrogen functionalization: (a) 1, (b) 2, (c) 3, and (d) 4. (Color code: C-brown, H-white, N-blue).

Energy = -1975.62 eV

Energy = -1529.51 eV

Energy = -1666.7 eV

Energy = -1678.39 eV
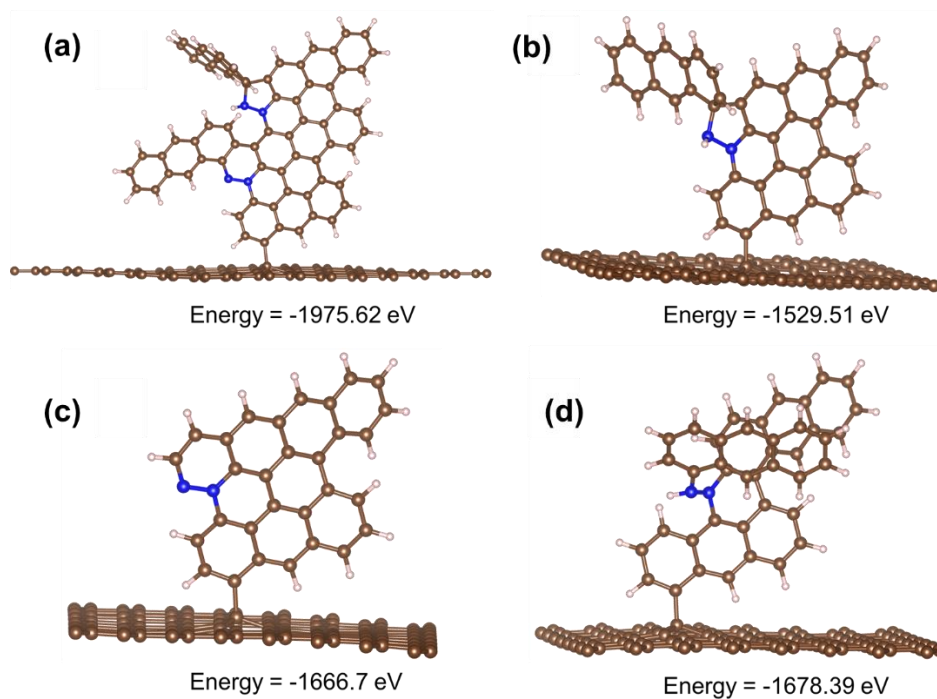
Fig S20. DFT optimized possible structures on graphene along with their corresponding energies: (a) 1@GR, (b) 2@GR, (c) 3@GR, and (d) 4@GR. (Color code: C-brown, H-white, N-blue).
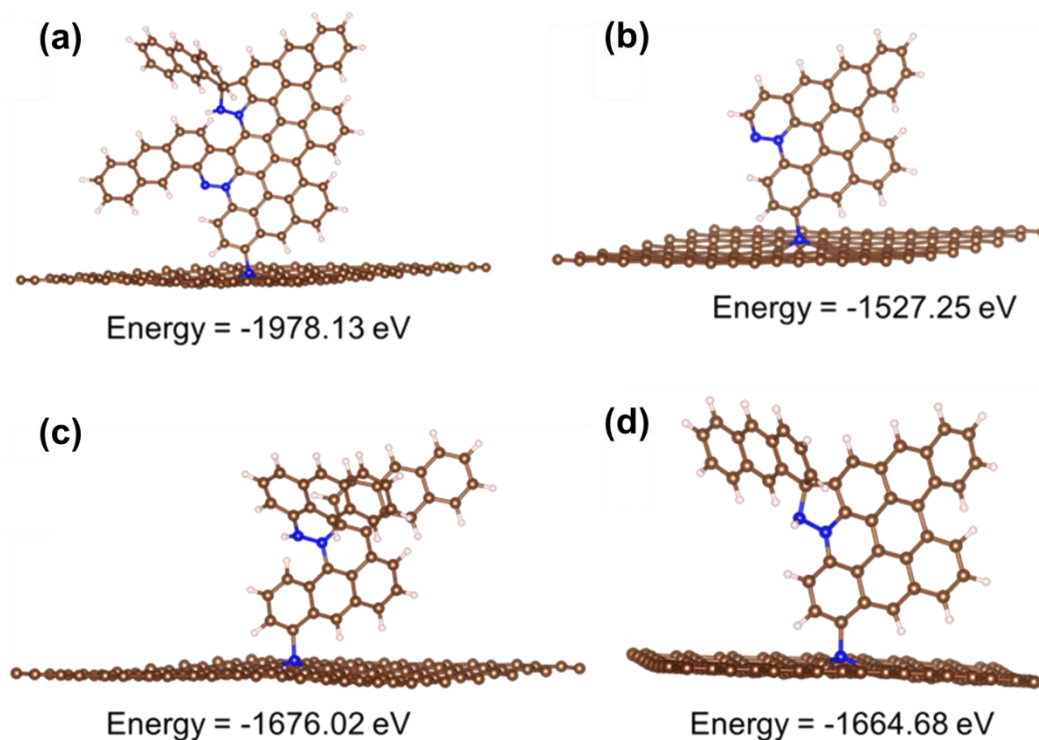
Fig S21. DFT optimized possible structures on N-doped graphene along with their corresponding energies: (a) 1@GR, (b) 2@GR, (c) 3@GR, and (d) 4@GR. (Color code: C-brown, H-white, N-blue).
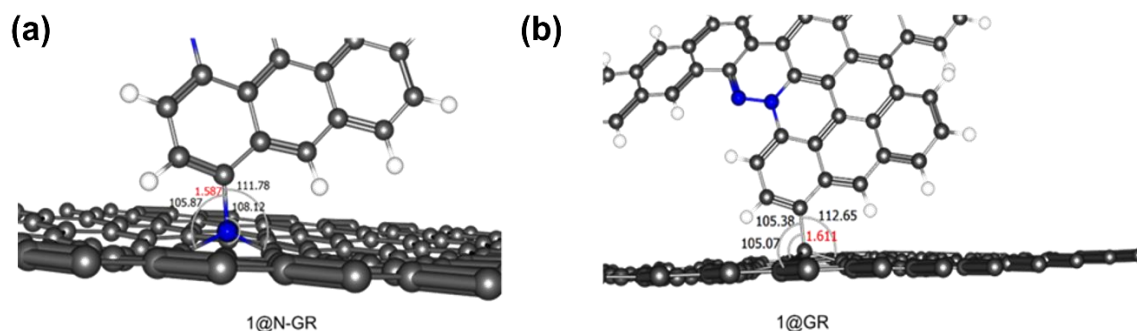
Fig S22. DFT optimized structure for (a) 1@N-GR and (b) 1@GR with relevant structural parameters. (Color code: C-brown, H-white, N-blue).
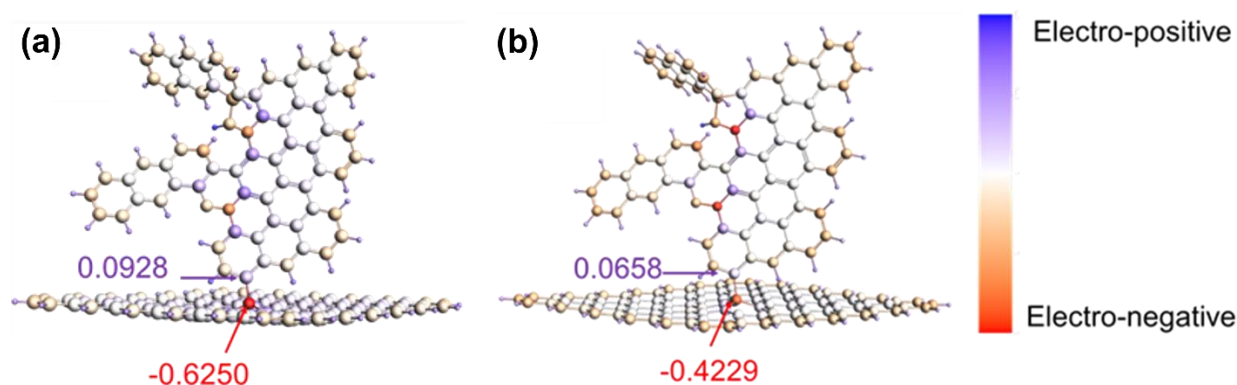
Fig S23. Plot of Mulliken charges on individual atoms being displayed in the order of their electro positivity/electronegativity for (a) 1@N-GR, and (b) 1@GR. (Red color shows electronegativity while blue shows electro positivity)
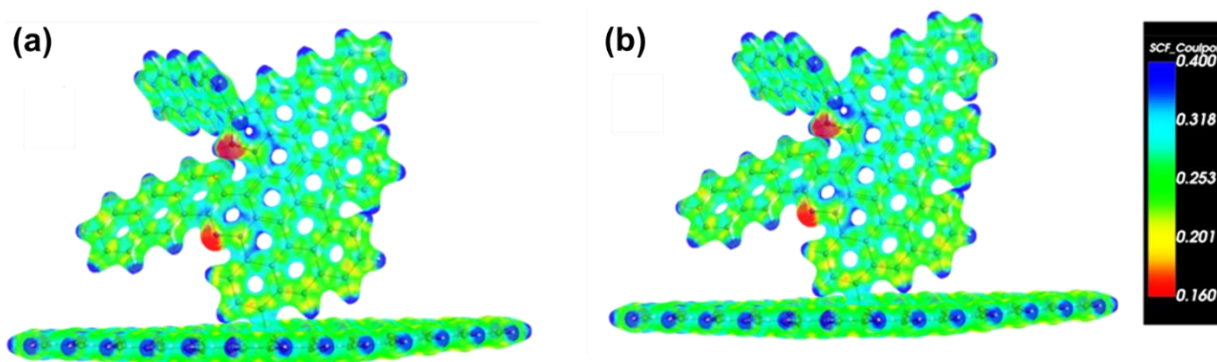
Fig S24. Electrostatic Potential Maps for (a) 1@N-GR, and (b) 1@GR. Red color shows electronegativity while blue shows electro-positivity.

Energy Decomposition Analysis

To get a better insight into the nature of the interaction between the complex and graphene/N-doped graphene, we made cluster models of some pDFT-optimised structures and performed EDA analysis[4,5] using the ADF 2021 software package. Single-point energy calculations were done at the PBE-D3(BJ)/DZ level of theory. In EDA,

$$\Delta E_{int} = \Delta E_{elstat} + \Delta E_{Pauli} + \Delta E_{orbital} + \Delta E_{disp}$$

Here, the term ΔE_{int} refers to the total bonding energy, ΔE_{elstat} corresponds to the electrostatic interaction (attractive), ΔE_{Pauli} refers to the Pauli repulsion energy, ΔE_{orb} accounts for orbital interactions resulting from electron pair bonding, charge transfer, and polarization terms, and ΔE_{disp} represents the dispersion interaction terms.

Table S6. Energy decomposition analysis for the modeled structures grafted on N-GR/GR calculated the PBE-D3BJ/DZ level of theory.

	E_{Elstat}	E_{Pauli}	E_{Orb}	E_{Disp}	E_{Int}
1@N-Gr	-185.1	351.7	-199.9	-21.3	-54.6
1@Gr	-156.6	307.8	-205.8	-18.0	-72.6

To theoretically elucidate the interactions between molecules and graphene, the ETS-NOCV technique was employed with DFT calculation. This technique combines the ETS method with the NOCV scheme, providing additional validation for the results mentioned earlier. Here, we have decomposed the orbital interaction term into Electron deformation densities corresponding to the highest interaction.

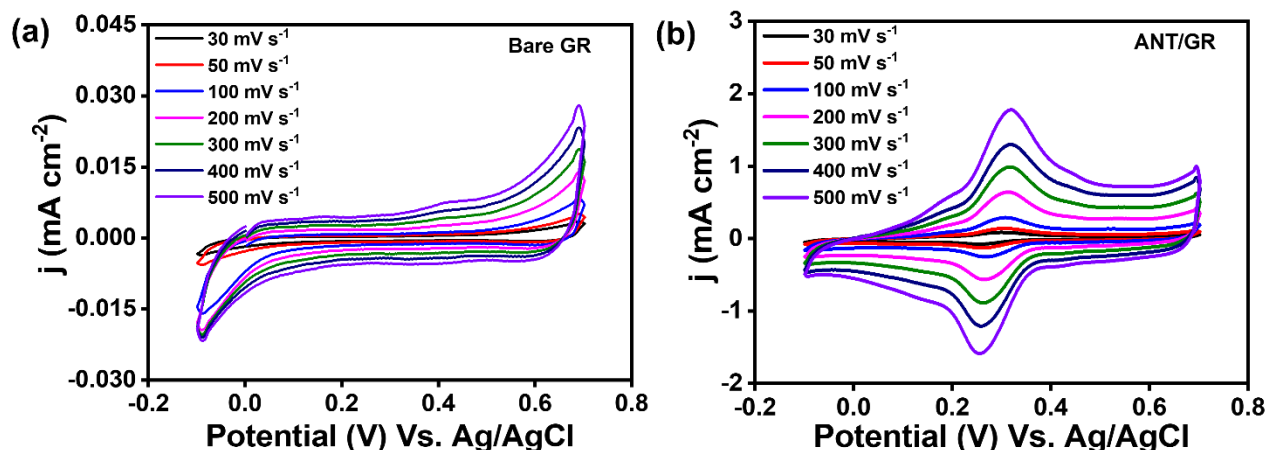## 11. CV of bare GR and ANT/GR at different scan rates

Fig S25. Cyclic Voltammograms of bare (a) GR, and (b) ANT/GR in 1 M H_2SO_4 aqueous solution at different scan rates.

12. Calculation for k_{app} for ANT/GR substrate

The rate of electron transfer at the ANT/GR electrode surface was calculated using Laviron formalism, as shown below.[6]

$$E_{P,C} = E^{\circ\prime} - \frac{2.3\,RT}{\alpha nF} \log\left[\frac{\alpha nFv}{RTk_{app}}\right] \tag{ii}$$

$$E_{P,a} = E^{\circ\prime} + \frac{2.3\,RT}{(1-\alpha)nF} \log\left[\frac{\alpha nFv}{RTk_{app}}\right] \tag{iii}$$

Eqs (ii) and (iii) are rearranged to show the trumpet plot equation.

$$E_{P,C} - E^{\circ\prime} = -\frac{2.3\,RT}{\alpha nF} \log\left[\frac{\alpha nFv}{RTk_{app}}\right]$$

$$E_{P,a} - E^{\circ\prime} = +\frac{2.3\,RT}{(1-\alpha)nF} \log\left[\frac{\alpha nFv}{RTk_{app}}\right]$$

Where $E_{p,c}$, and $E_{p,a}$ are the potential of the cathodic and anodic peaks. $E^{\circ\prime}$ is the formal potential calculated by taking the average of the anodic and cathodic potentials at a low scan rate, v is the scan rate, α is the electron transfer coefficient, k_{app} is the apparent rate constant, T is the absolute temperature, R is the ideal gas constant, F is the Faraday constant, and n is the number of electrons transferred. Electron transfer parameters such as v_a, v_c, α, and k_{app} are calculated by plotting the plot between $Ep - E^{\circ\prime}$ vs. log of the scan rate, known as the trumpet plot. The critical scan rates v_c and v_a are determined by extrapolating the linear portion to 0 V, and α is deduced from the slope of the linear part. CV was performed to analyze these parameters using ANT/GR as a working electrode in 1 M H_2SO_4 electrolyte from 30 mV/s to 10 V/s scan rate.
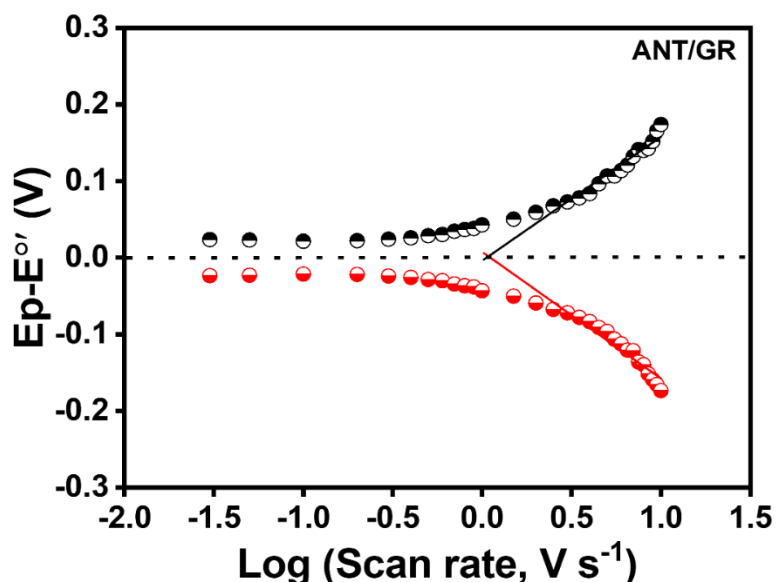
Fig S26. Trumpet plot of ANT/GR in 1 M H_2SO_4 solution.

Calculation for α and 1- α from the above trumpet plot

Cathodic fit obtained from linear fit: y = −0.1653x + 0.0076

Anodic fit obtained from linear fit: y = 0.1617x − 0.0040

$$\text{Slope}_c = -\frac{2.3\ RT}{\alpha nF} \qquad\qquad \text{Slope}_a = +\frac{2.3\ RT}{(1-\alpha)nF}$$

Putting slope value from cathodic and anodic fit

α = 0.35   1- α = 0.36

Calculation for v_c and v_a

$$\log (v) = -\frac{y-intercept}{slope}$$

$v_c = 1.1$ V/s $v_a = 1.0$ V/s

Calculation for k_{app} using the above-calculated parameters

$$k_{app,c} = \frac{\alpha nF v_c}{RT} \qquad\qquad\qquad k_{app,a} = \frac{(1-\alpha)nF v_a}{RT}$$

$k_{app,c} = 14.9$ s^{-1} $k_{app,a} = 14.0$ s^{-1}

13. Calculation for diffusion coefficient (*D*) for bare GR and ANT/GR electrode using ferrocene as a redox probe

To calculate the diffusion coefficient value of ferrocene, CV was performed using bare GR and ANT/GR as working electrodes in 5 mM ferrocene solution in acetonitrile (ACN) with TBAP as supporting electrolyte at a scan rate of 100 mV s^{-1}.
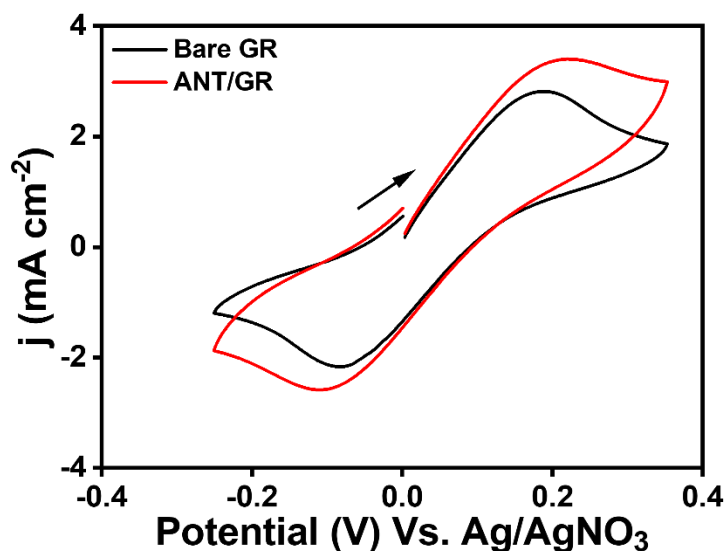
Fig S27. CV of bare GR and ANT/GR electrode in 5 mM ferrocene in ACN with 0.1 M TBAP as supporting electrolyte at 100 mV s^{-1} scan rate.
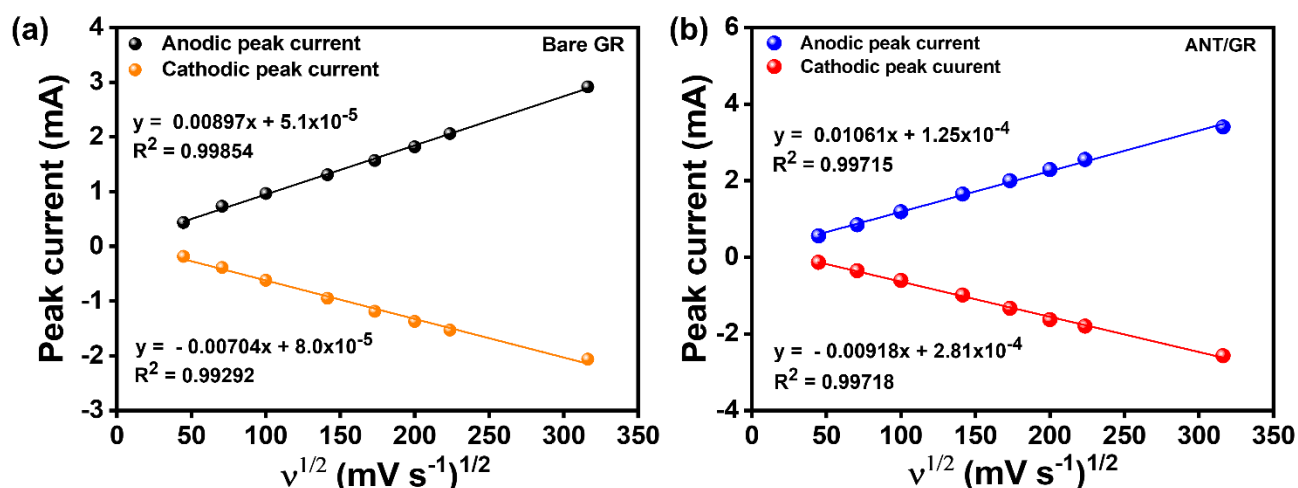
Fig S28. Peak current as a function of square root of scan rate for (a) bare GR, and (b) ANT/GR.

14. Thermal stability of ANT/GR interfaces

To study the temporal stability of the ANT/GR electrode, electrolyte temperature was varied from 5° C to 50° C. Temperature increase has led to a minor effect on the peak current of the ANT/GR electrode.

From the Arrhenius equation, activation energy (E$_a$) can be determined. From Eq (iv), k can be expressed as current density.[7] **Fig S29** shows the log j vs. 1000/T plot of ANT/GR, and the E$_a$ was calculated to be 10.94 kJ mol^{-1}.

$$k = A\, e^{-E_a/RT} \qquad\qquad \text{(iv)}$$

$$\log k = \log A - \frac{E_a}{2.303\, RT} \qquad\qquad \text{(v)}$$
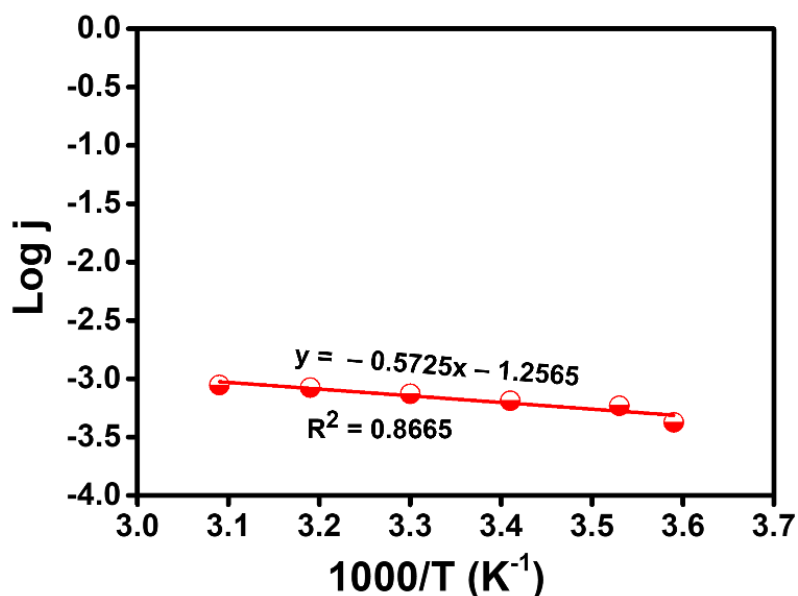
Fig S29. Plot of log j vs. 1000/T at different electrolyte temperatures on the ANT/GR electrode.

ANT/GR electrode was also heated at 75°C for 12 h to check the stability of the modified GR. No significant changes are observed even on heating the electrode, suggesting the higher temporal stability of the modified electrode.
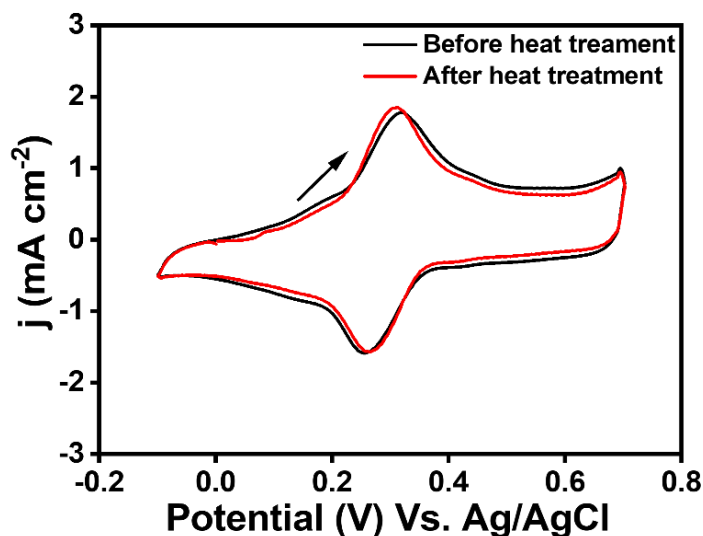
Fig S30. Cyclic Voltammograms of ANT/GR in 1 M H_2SO_4 aqueous solution at 500 mV s^{-1} scan rate before and after heat treatment at 75° C for 12 h.

15. Calculation for total capacitance of bare GR, modified GRs

The total areal capacitance was determined by integrating the area enclosed by CVs according to Eq. (vi).

$$C = \frac{Q}{\Delta E} \qquad \text{(vi)}$$

Where Q = Total integrated absolute area/scan rate

ΔE = Potential range
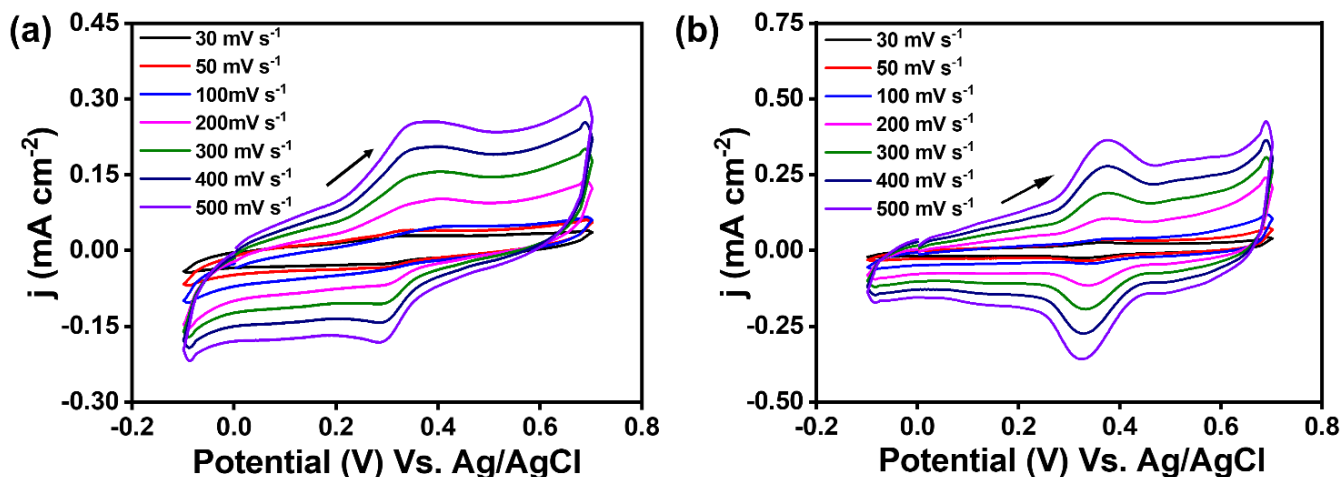
Fig S31. Cyclic Voltammogram of (a) NAPH/GR, and (b) PYR/GR recorded in 1 M H_2SO_4 aqueous solution at different scan rates.
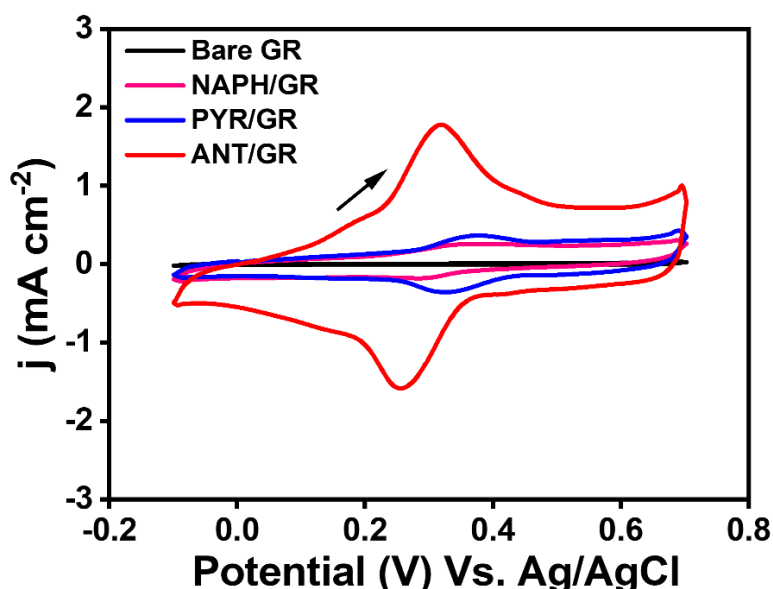
Fig S32. Comparison of cyclic Voltammogram of bare GR, NAPH/GR, PYR/GR, and ANT/GR in 1 M H_2SO_4 aqueous solution at 500 mV s^{-1} scan rate.

16. Theoretical weight calculation for ANT film on GR substrate

Since it is very challenging to determine the mass loading of the grafted nanoscale ANT film (active material) experimentally on GR substrate, we theoretically estimated the mass loading of the ANT film on GR substrate. We first determined the volume of the thin film with the help of area and thickness of the film. The thickness of the ANT film was determined by AFM analysis. For the area of the film, we considered the geometrical area of the electrode.

Area of the thin film = 1.256 cm^2,

Thickness of the thin film = 24 nm

Putting these values into Eq. (vii)

Volume = Area of thin film × Thickness   (vii)

Volume was calculated to be 3.014 µcm^3.

Assuming the density (d) of the bulk Anthracene (ANT) close to the ANT thin film, according to Eq. (viii), we estimated the mass of the active material (ANT thin film) to be 3.76 µg.

$$d = 1.25 \text{ g cm}^{-3}, V = 3.014 \text{ µcm}^3$$

$$d = \frac{m}{V} \qquad\qquad (viii)$$

17. Current density vs. scan rate plot for bare GR and modified GR

The capacitance at constant potential is calculated by using the Eq. (ix).

$$C = \frac{j}{scan\ rate} \qquad\qquad (ix)$$

Where j = current density at the selected potential
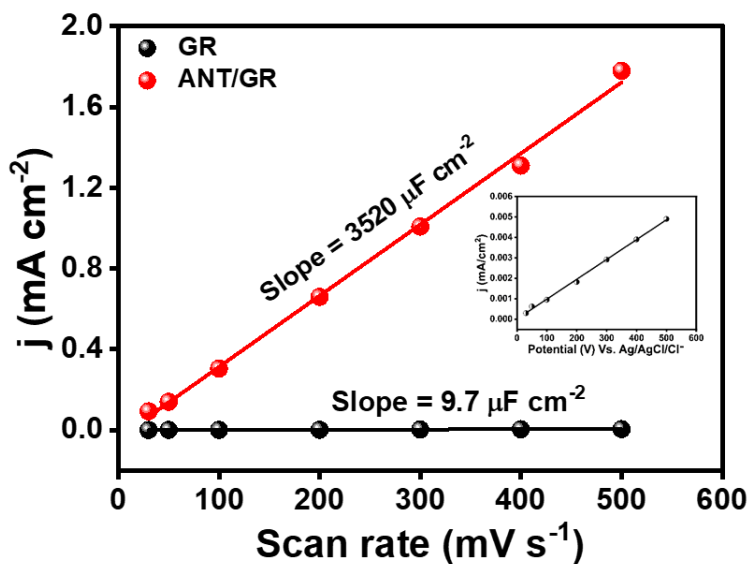
Fig S33. Scan rate vs. current density plot of bare GR, and ANT/GR at a constant potential of 0.31 V Vs. Ag/AgCl inset showing scan rate vs. current density plot of bare GR.
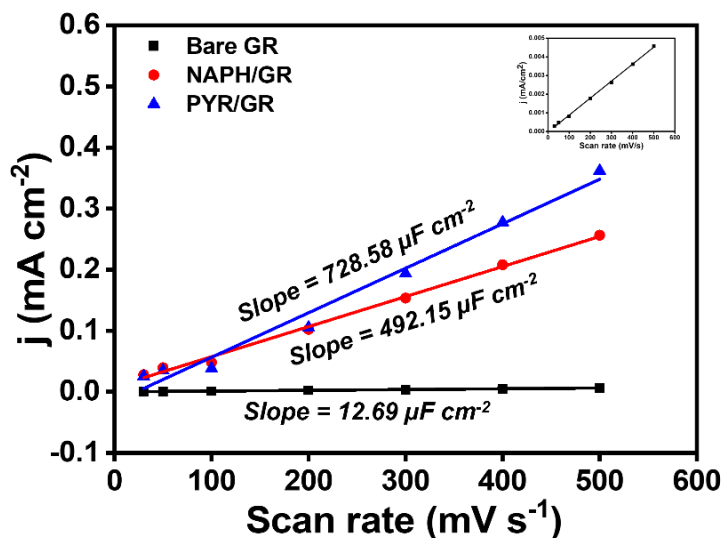
Fig S34. Scan rate vs. current density plot of bare GR, NAPH/GR, and PYR/GR at a constant potential of 0.38 V Vs. Ag/AgCl inset showing scan rate vs. current density plot of bare GR.
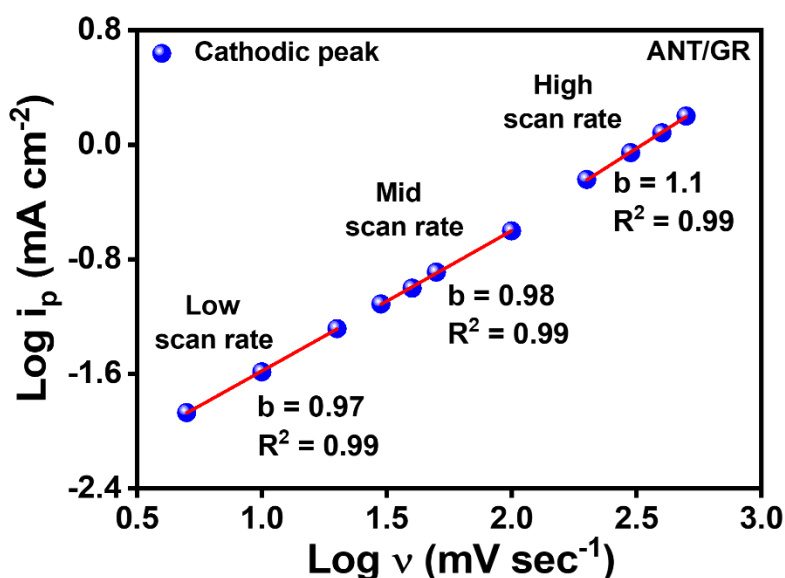
Fig S35. Plots of log (i_p) vs. log (υ) from low to high scan rates for ANT/GR electrode in the cathodic regime.

18. Constant galvanostatic charge/discharge (GCD) measurements for bare GR and ANT/GR

Constant GCD measurement of bare GR and ANT/GR was performed using the Autolab workstation. Ten GCD cycles were measured for both samples at an applied current density of 30 μA cm^{-2}. Areal capacitance was calculated by using Eq. (x).

$$C = \frac{j \times t_D}{\Delta E} \qquad (x)$$

Where j = areal and specific current density; t_D = discharge time; ΔE = Potential window.

A single GCD cycle of bare and ANT/GR at an applied current density of 30 µA cm^{-2} is shown in **Fig S36**. In bare GR, charging and discharging time were calculated to be 3 s and 4 s, respectively, which increased after ANT modification to 53 s and 66 s.
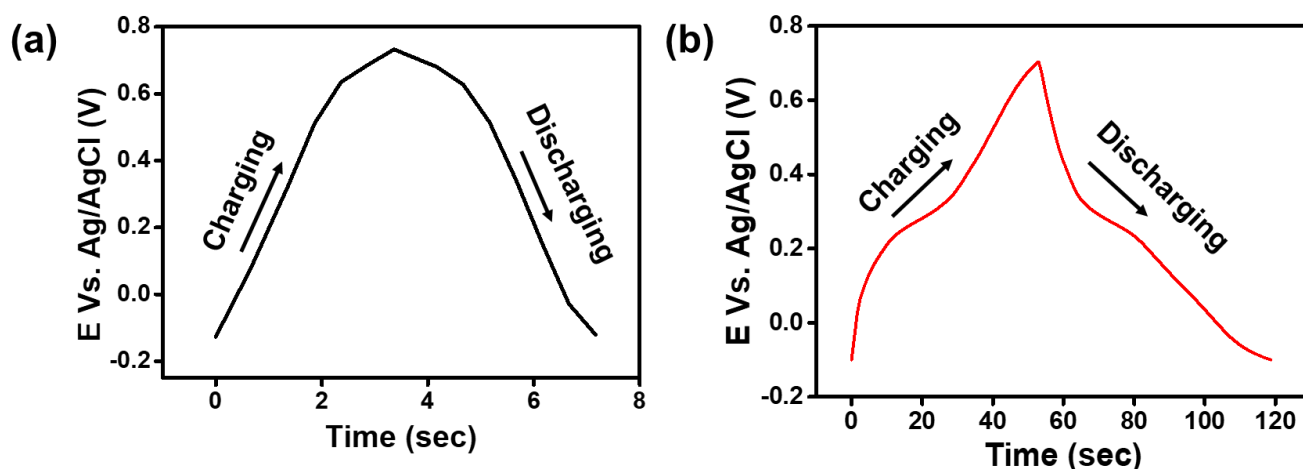
Fig S36. A single GCD cycle of (a) bare GR, and (b) ANT/GR at an applied current density of 30 µA cm^{-2}.

Calculation of equivalent series resistance (ESR):

The drop in voltage between the end of charging and the start of discharging GCD cycle is a potential drop V_{drop}. This drop occurs due to the ESR (equivalent series resistance) of the cell. ESR is calculated by using Eq. (xi).

$$ESR = \frac{V_{drop}}{J} \qquad \text{(xi)}$$

For cyclic stability, GCD measurement was done up to 10^4 charging/discharging cycles. The ANT/GR underwent 10^4 charging/discharging cycles between −0.1 to + 0.7 V vs. Ag/AgCl at an applied current density of 1 mA cm^{-2}. After every 10^3 cycles, a single GCD cycle was plotted to determine the capacitance. A similar approach was performed for bare GR as well; however, to ensure the experiment time was the same for both ANT/GR and bare GR, 0.1 mA cm^{-2} current density was applied.[8]
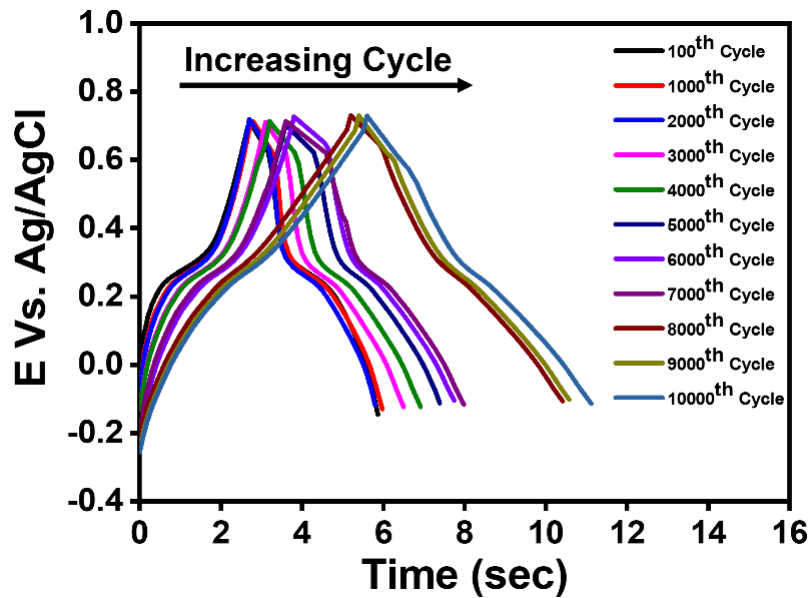
Fig S37. Comparison of GCD plots of ANT/GR for 10^4 charging/discharging cycles between -0.1 to $+0.7$ V vs. Ag/AgCl at an applied current density of 1 mA cm^{-2}, plotted for every 10^3 cycles.

Calculation of coulombic efficiency (CE):

The coulombic efficiency (η) was calculated from a GCD plot using Eq. (xii).[9]

$$\eta = \frac{t_d}{t_c} \times 100 \ \% \qquad \text{(xii)}$$
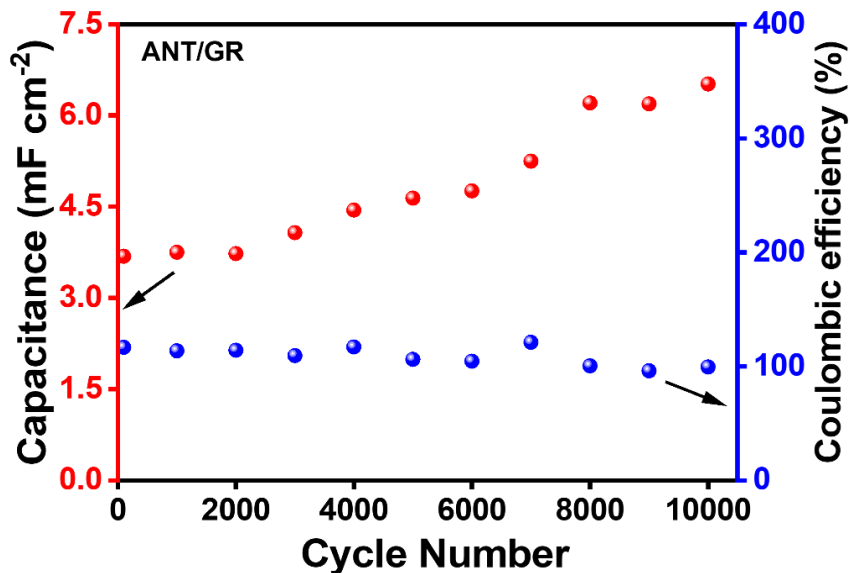
Fig S38. Areal capacitance and coulombic efficiency (%) vs. GCD cycle number plot for ANT/GR electrode.

19. Microscopic and spectroscopic characterization of ANT/GR after 10^4 GCD cycles
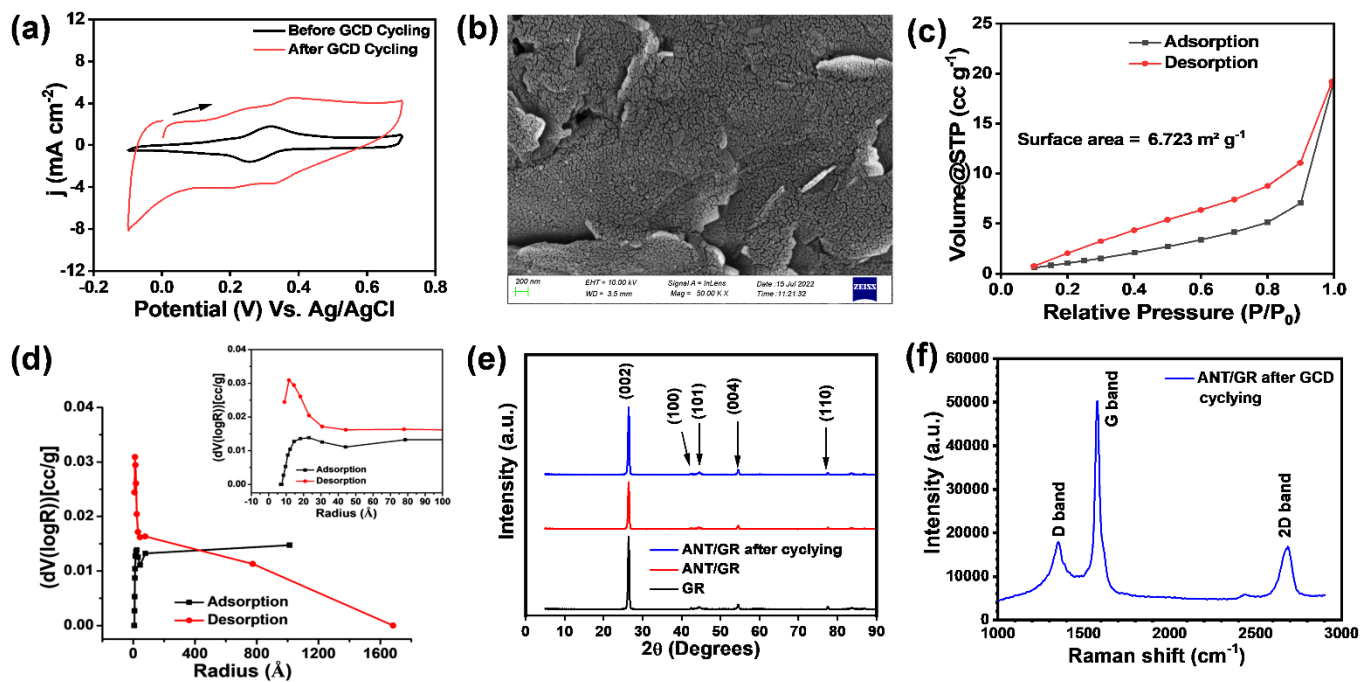
Fig S39. (a) CV of ANT/GR in 1 M H_2SO_4 before (black) after 10^4 GCD cycles (red), (b) FE-SEM image of ANT/GR electrode after 10^4 GCD cycles, (c) Nitrogen adsorption-desorption isotherm, (d) Pore size distribution of ANT/GR electrode after 10^4 GCD, (e) XRD pattern of ANT grafted thin films on GR electrode before and after 10^4 GCD cycles, and (f) Raman spectra of ANT/GR after 10^4 GCD cycles.
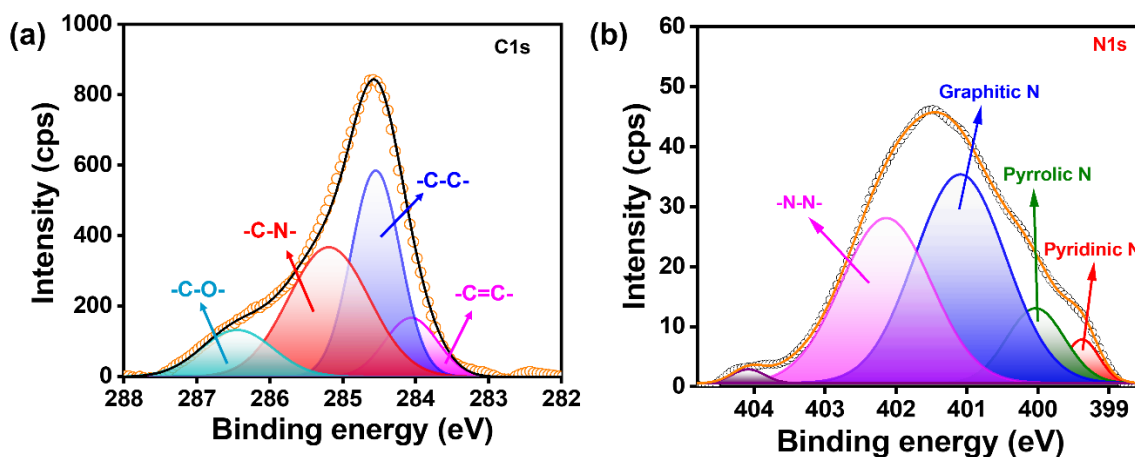
Fig S40. Deconvoluted and fitted XPS spectra of (a) C1s, and (b) N1s of ANT/GR after 10^4 GCD cycling.
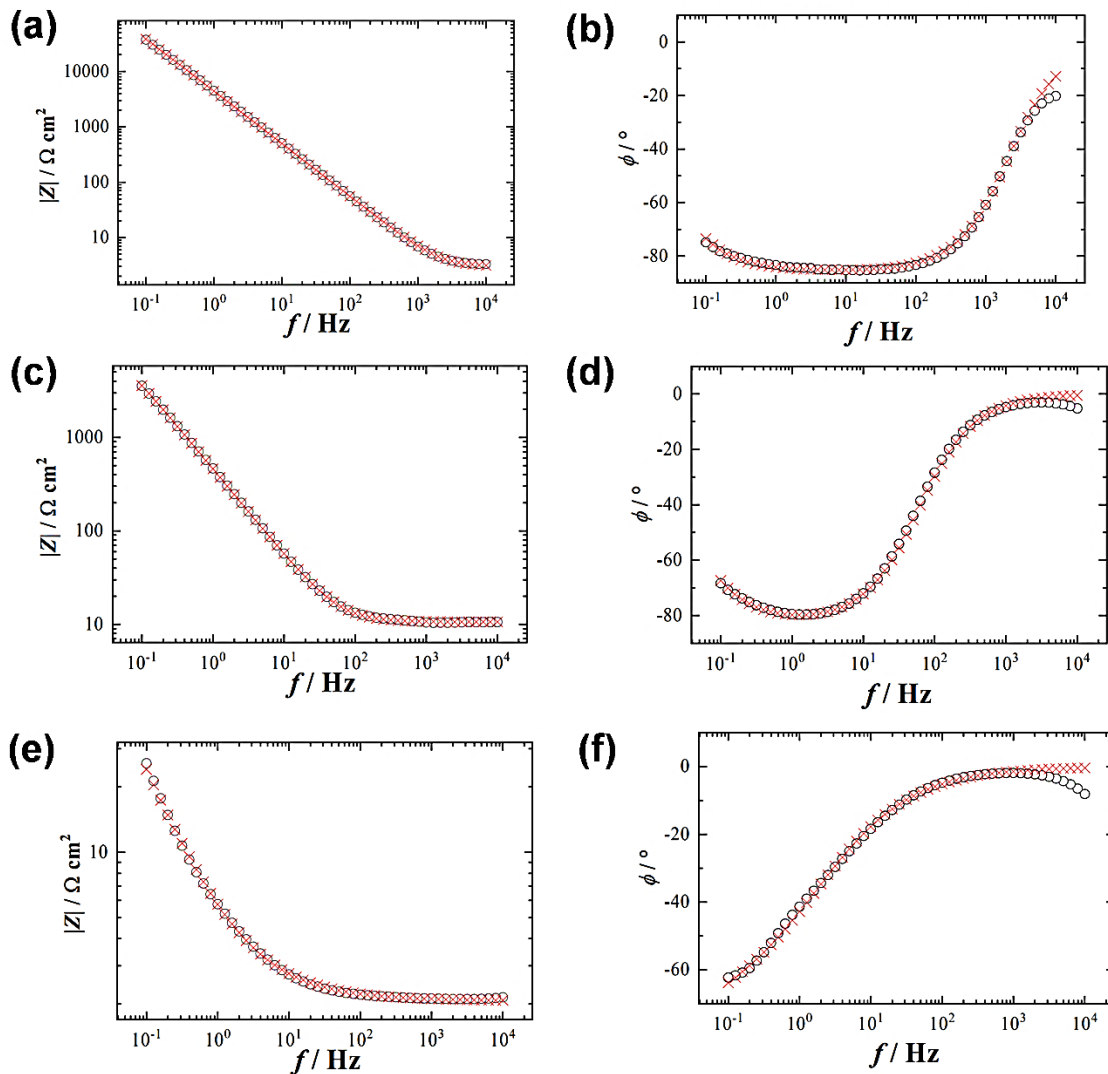
Fig S41. Graphical fitting of bode plot of (a-b) bare GR, (c-d) ANT/GR, and (e-f) ANT/GR after 10^4 GCD cycling.

Table S7. Electrochemical parameters obtained after graphical fitting.

Serial No.	Sample	R_e (Ω cm^2)	R_{ct} (Ω cm^2)	Q_{HF} (Fs$^{(\alpha-1)}$ cm^{-2})	α_{HF}	Q_{LF} (Fs$^{(\alpha-1)}$ cm^{-2})	α_{LF}
1.	Bare GR	2.98	-	3.92×10^{-5}	0.95	-	-
2.	ANT/GR	10.62	13284	3.99×10^{-4}	0.92	-	-
3.	ANT/GR after GCD cycling	2.064	199.3	8.62×10^{-2}	0.66	2.0×10^{-2}	0.81

R_e = Electrolyte resistance, R_{ct} = charge transfer resistance, Q_{HF} = CPE parameter at high-frequency limit, Q_{LF} = CPE parameter at low-frequency limit, α_{HF} = CPE exponent at high-frequency limit, α_{LF} = CPE exponent at low-frequency limit

20. Electrochemical study of ANT/EV-GR (GR isolated from discharged Eveready cell)

We have isolated EV-GR from a used dry cell, as shown in **Fig S42**; afterward, we cleaned it by sonication in acetone for 35 minutes, then in distilled water for 35 minutes, and dried at 60 °C for 12 h in the oven. After cleaning, the EV-GR was used for E-Chem grafting.
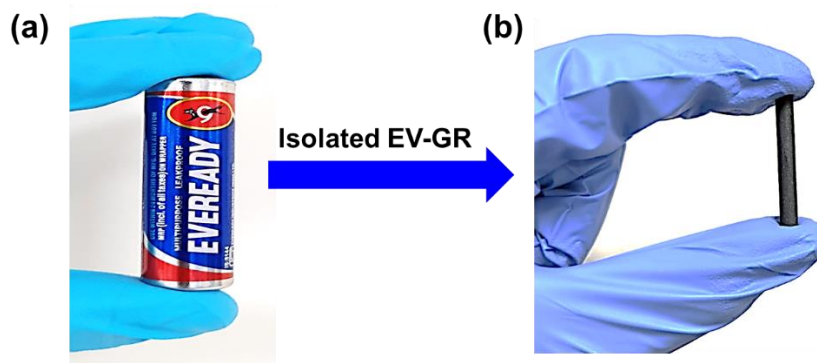
Fig S42. Digital image of (a) EV-cell, and (b) graphite rod isolated from used Eveready dry cell.
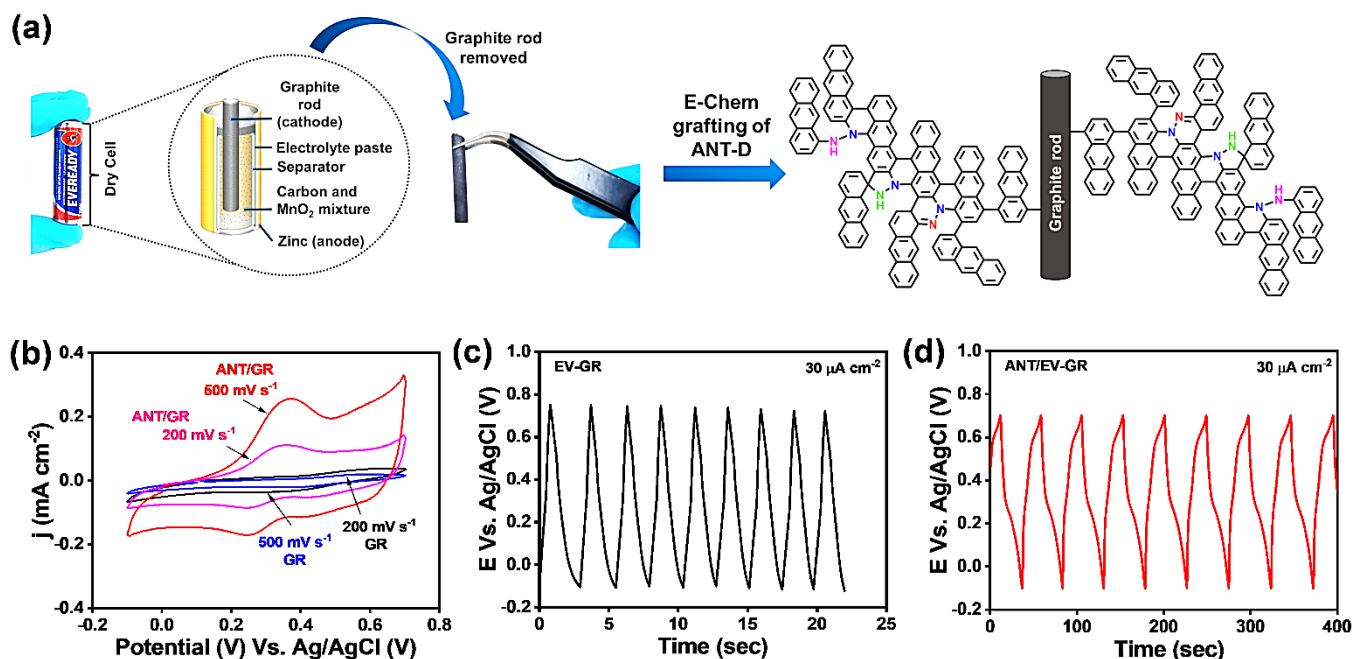
Fig S43. (a) Schematic illustration of E-Chem modification of graphite rod isolated from an Eveready cell using anthracene diazonium. (b) Cyclic voltammograms of EV-GR and ANT/EV-GR in 1 M H_2SO_4. (c) GCD curves of EV-GR and (d) ANT/EV-GR at 30 µA cm^{-2} applied current density for nine cycles.

21. Electrical conductivity of bare GR and ANT/GR

The conductivity of bare GR and ANT-modified GR was measured by connecting a single graphite rod/modified GR between two crocodile clips (the length of all GR was kept the same). The resistance of bare GR was calculated to be 1.4 Ω. After ANT modification, the rod's resistance was bit increased to 3 Ω, which on 10^4 GCD cycling decreased to 1.8 Ω, showing the excellent conducting feature of the modified electrode.
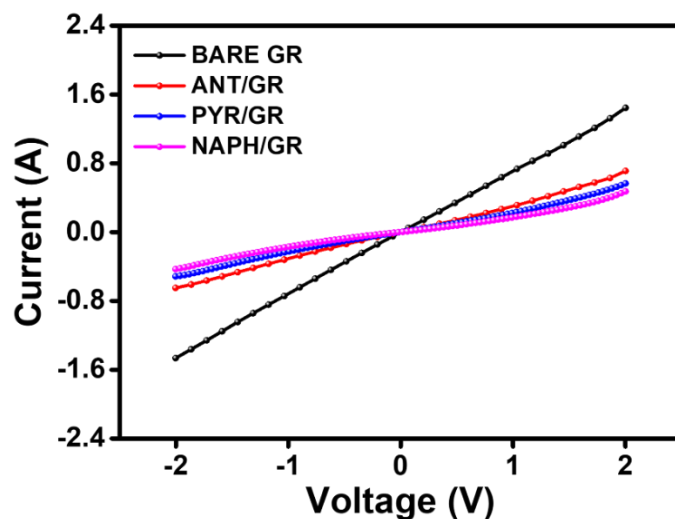
Fig S44. Current vs. voltage plot (two probe contact electrical measurements using a Keithley source meter) of bare GR (black), ANT/GR (red) electrode, PYR/GR (blue), and NAPH/GR (pink).
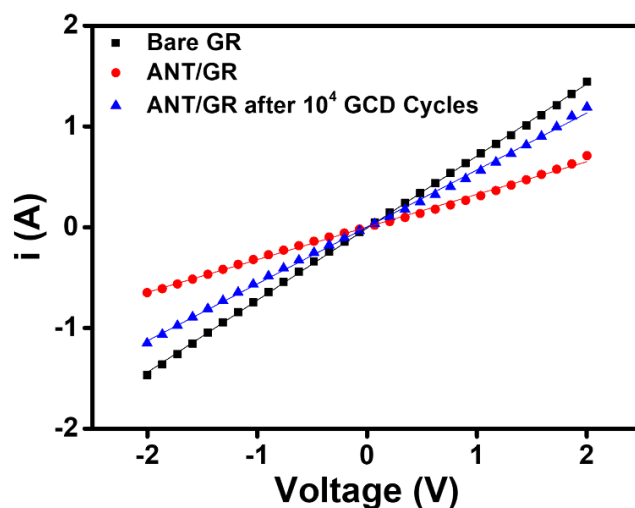
Fig S45. Current vs. voltage plot (two probe contact electrical measurements using a Keithley source meter of bare GR (black), ANT/GR (red) electrode, and after 10^4 GCD cycles (blue).

22. Fabrication of solid-state asymmetric supercapacitor devices via spontaneous grafting of D-ANT.

In order to assemble an asymmetric supercapacitor (ASC) device, ANT-grafted porous carbon (ANT/PC) and porous carbon (PC) was used as a positive and a negative electrode, and a Whatman filter paper soaked with 1 M H_2SO_4 was used as a separator as shown in **Fig S46a**. Asymmetric configuration was opted to increase the potential window of the device, hence increasing the energy density of the device. For this purpose, we used porous carbon (PC) derived from environment-friendly and widely available coconut fiber. The synthesis and characterization of PC can be found in our previous paper.[10] Next, 60 mg of PC was dissolved in 30 mL of DI water and sonicated for 1 h. Afterward, anthracene diazonium (D-ANT) salt (88 mg) was added to it. Solution pH = 11-12 was maintained by adding a few drops of 2 M NaOH and heated at 60° C for 2 h. The product was collected by centrifugation and dried at 50° C. Following that, the positive electrode consists of a composite electrode prepared by mixing ANT/PC (60 %), PC (30 %), and polyvinylidene fluoride (PVDF, 10 %) with N-methyl-2-pyrrolidone (NMP, 1 mL) to form a homogeneous

slurry. The slurry was uniformly coated on stainless steel (2×2 cm^2) and dried. Similarly, PC (90 %) and polyvinylidene fluoride (PVDF, 10 %) were mixed with NMP (1 mL) to form a homogeneous slurry. The slurry was uniformly coated on stainless steel, dried, and used as negative electrode. The total areal mass loading of the electrodes was 0.14 mg cm^{-2}.
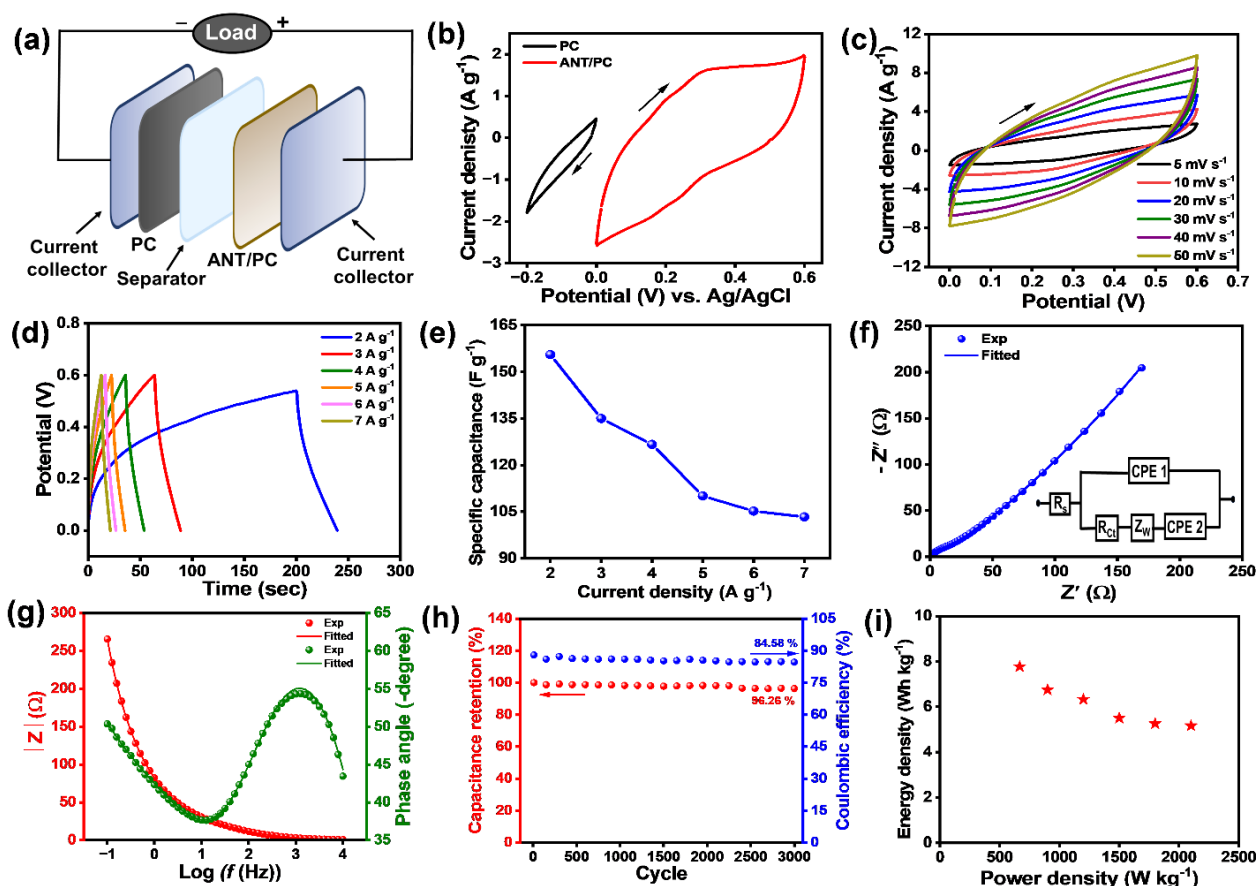
Fig S46. (a) Schematic illustration of asymmetric supercapacitor (ASC) device, (b) CV of ANT/PC and PC recorded in a three-electrode system at 20 mV s^{-1} scan rate in 1 M H$_2$SO$_4$ electrolyte solution, (c) CV of the ASC device at different scan rates, (d) GCD curve of the ASC device at different current densities and (e) respective specific capacitance values, (f) Nyquist, and (g) bode plot of the ASC device, (h) cyclic stability of the ASC device, and (i) Ragone plot of the ASC device.

The individual potential of both electrodes was determined by performing CV in a three-electrode system in 1 M H$_2$SO$_4$ electrolyte solution (**Fig S46b**). Similar to the ANT/GR electrode, a Faradaic peak at ~ 0.28 V vs. Ag/AgCl was observed in ANT/PC. Next, CV curves were recorded for the device at different scan rates (**Fig S46c**). The continuous stability of CV curves, even at high scan rates, indicates good reversibility, exceptional rate capabilities, and remarkable device stability. **Fig S46d** shows the GCD curve of the device at different current densities, and their corresponding specific capacitance is shown in **Fig S46e**. The GCD curve shows a nearly triangular shape with a small plateau region, as expected for the typical ASC device. Further, Electrochemical impedance measurement was performed in the frequency range from 10^4 Hz to 0.1 Hz at 5 mV amplitude with zero DC voltage. The Nyquist plot is shown in **Fig S46f** with a small semicircle in the low-frequency region, indicating low charge transfer resistance (R$_{ct}$). The non-zero

intersection at the real impedance axis in the Nyquist is the uncompensated series resistance (R_S), which includes the ionic resistance of the electrolyte, intrinsic resistance of the active materials (ANT/PC), and the contact resistance at the interface between the active electrode material and current collector stainless steel. The Nyquist plot was fitted with an equivalent circuit model, as shown in the inset of **Fig S46f**.[11,12] In the equivalent circuit, the uncompensated series resistance (R_s) is connected in series with a constant phase element (CPE 1) Q, which is connected in parallel with the charge transfer resistance (R_{Ct}). The Warburg diffusion element connected in series with R_{Ct} is used to show a transition from high to low-frequency region and is represented by Z_W, which corresponds to the diffusion of the electrolyte ions through the active material. Also, at very low frequencies, another constant phase element (CPE 2) was used, leading to a deviation from a straight line parallel to the imaginary axis due to the PCET reaction. A similar observation was well reflected in the bode plot (**Fig S46g**). The fitted values are shown in **Table S8.**

Table S8. Electrochemical parameters obtained after fitting with the suggested circuit model.

Sample	R_s (mΩ cm^2)	R_{ct} (Ω cm^2)	Q_1 (μFs$^{(\alpha-1)}$ cm^{-2})	α_1	Q_2 (mFs$^{(\alpha-1)}$ cm^{-2})	α_2	Z_W (mΩ s$^{-0.5}$)
ASC device	277	20.7	538	0.73	37.7	1.0	5.03

Moreover, the stability of the ASC device was also examined, and the device was stable up to 3×10^3 GCD cycles with 96 % capacitance retention and 85 % coulombic efficiency (**Fig S46h**). By using Eqs. (xiii) & (xiv), the energy density and power density of the ASC device were determined.[13–16] The values are displayed in the Ragone plot (**Fig S46i**). The obtained specific capacitances for both the ANT grafted electrodes, ANT/GR, and ANT/PC are significantly better than most values previously reported for carbon materials functionalized with organic molecules by using the diazonium modification method. **Table S9** compares the specific capacitances, energy density, and power density of the carbon materials functionalized with organic molecules using the diazonium modification method.

$$E_A = \frac{1}{2} C_A \times (\Delta V)^2 \times \frac{1}{3.6} \qquad \text{(xiii)}$$

$$P_A = \frac{E_A}{t_D} \times 3600 \qquad \text{(xiv)}$$

Where C_A = capacitance calculated from the GCD curve

ΔV = Potential window; t_D = discharge time

Table S9. Comparison of electrochemical charge storing performance of carbon materials factionalized with organic molecules by diazonium reduction process.

Electrode	Electrolyte	Measurement condition	Specific capacitance	Energy density	Power density	Ref
Anthraquinone Modified carbon fabric	1 M H_2SO_4	1 mV s^{-1}	1470 F g^{-1}	1.13 Wh kg^{-1}	6.18 W g^{-1}	[17]
Anthraquinone Modified activated carbon	0.1 M H_2SO_4	10 mV s^{-1}	195 F g^{-1}	-	-	[5]
Phenanthrenequinone modified porous carbon	1 M KOH	2 A g^{-1}	180 C g^{-1}	-	-	[18]
Catechol-modified activated carbon	1 M H_2SO_4	2 mV s^{-1}	250 F g^{-1}	-	-	[19]
Tetrahydrozyphenazine-modified activated carbon	1 M H_2SO_4	1 A g^{-1}	180 C g^{-1}	-	-	[20]
Naphthalene-modified graphene ribbon (GR) on PPF	0.1 M H_2SO_4	27 µA cm^{-2}	1238 µF cm^{-2}	-	-	[8]
GR/XCmax22 carbon black		2 A g^{-1}	950-1892 F g^{-1}	318 Wh kg^{-1}	> 40 Wkg^{-1}	
Carboxy benzene-modified carbon paper	1 M Na_2SO_4	0.5 A g^{-1}	447 F g^{-1}	4.8 Wh kg^{-1}	1920 W kg^{-1}	[21]
Nitrobenzene-modified activated carbon	1 M KOH	5 mV s^{-1}	129 C g^{-1}	-	-	[20]
Nitrobenzene modified graphene	6 M KOH	0.1 V s^{-1} 3 mA cm^{-2}	71 F g^{-1} 17 mF cm^{-2}	-	-	[22]
Naphthalene modified graphite rod (NAPH/GR)	1 M H_2SO_4	0.5 V s^{-1}	516 µF cm^{-2}	-	-	This work
Pyrene-modified graphite rod (PYR/GR)	1 M H_2SO_4	0.5 V s^{-1}	726 µF cm^{-2}	-	-	
Anthracene modified graphite rod (ANT/GR)	1 M H_2SO_4	0.5 V s^{-1}	2506 µFcm^{-2}	-	-	
		10 µA cm^{-2}	11 mF cm^{-2} 2900 F g^{-1}	-	-	
Anthracene-modified biomass-derived porous carbon (ANT/PC)	1 M H_2SO_4	2 A g^{-1}	155 F g^{-1}	5.8 Wh kg^{-1}	2010 W kg^{-1}	

Four ASC devices with areal mass loading of ~ 0.45 mg cm^{-2} (for each device) were connected in series to light up the LED. The device was charged with a 6 V battery for 2 minutes, and the LED lit-up time was 5 ± 0.8 minutes (**Fig S47**).
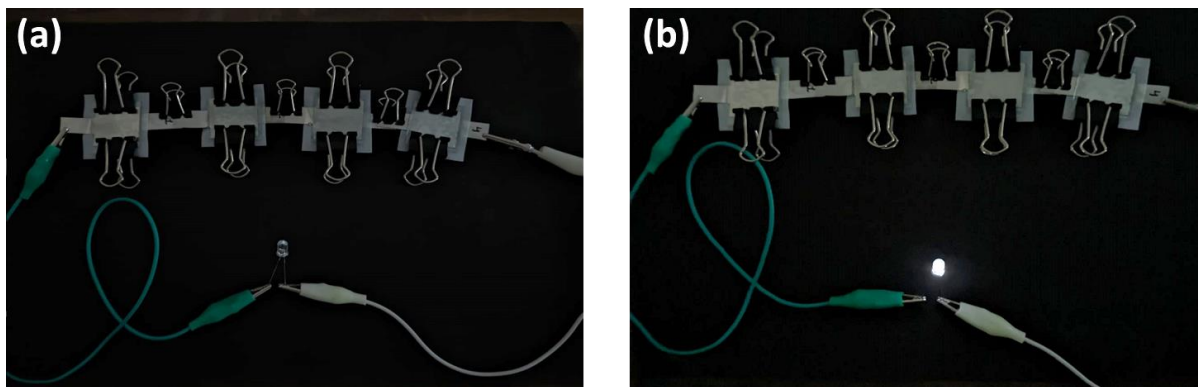
Fig S47. Four ASC devices connected in series (a) before charging and (b) after charging with a 6 V battery for 2 minutes.

21 References

1   A. Menon, J. A. H. Dreyer, J. W. Martin, J. Akroyd, J. Robertson and M. Kraft, *Phys. Chem. Chem. Phys.*, 2019, **21**, 16240–16251.

2   G. Kresse and J. Furthmüller, *Comput. Mater. Sci.*, 1996, **6**, 15–50.

3   G. Kresse and J. Furthmüller, *Phys. Rev. B - Condens. Matter Mater. Phys.*, 1996, **54**, 11169–11186.

4   M. P. Mitoraj, A. Michalak and T. Ziegler, *J. Chem. Theory Comput.*, 2009, **5**, 962–975.

5   M. P. Mitoraj, M. Parafiniuk, M. Srebro, M. Handzlik, A. Buczek and A. Michalak, *J. Mol. Model.*, 2011, **17**, 2337–2352.

6   E. Laviron, *J. Electroanal. Chem.*, 1979, **101**, 19–28.

7   M. F. Nazarudin, Z. Zainal, W. T. Tan, I. Hamadneh and E. F. Kadri, *Int. J. Electrochem. Sci.*, 2012, **7**, 2965–2982.

8   A. K. Farquhar, M. Supur, S. R. Smith, C. Van Dyck and R. L. McCreery, *Adv. Energy Mater.*, 2018, **8**, 1–9.

9   M. Beidaghi and Y. Gogotsi, *Energy Environ. Sci.*, 2014, **7**, 867–884.

10   P. Makkar, A. Malik and N. N. Ghosh, *ACS Appl. Energy Mater.*, 2021, **4**, 6015–6024.

11   T. Purkait, G. Singh, D. Kumar, M. Singh and R. S. Dey, *Sci. Rep.*, 2018, **8**, 1–14.

12   F. Barzegar, A. Bello, D. Momodu, M. J. Madito, J. Dangbegnon and N. Manyala, *J. Power Sources*, 2016, **309**, 245–253.

13   K. Chhetri, A. P. Tiwari, B. Dahal, G. P. Ojha, T. Mukhiya, M. Lee, T. Kim, S. H. Chae, A. Muthurasu and H. Y. Kim, *J. Electroanal. Chem.*, 2020, **856**, 113670.

14   J. Kunwar, D. Acharya, K. Chhetri, B. Karki, B. Deo, R. M. Bhattarai, S. Neupane, M. P. Adhikari and A. P. Yadav, *J. Electroanal. Chem.*, 2023, **950**, 117915.

15   K. Chhetri, A. Adhikari, J. Kunwar, D. Acharya, R. M. Bhattarai, Y. S. Mok, A. Adhikari, A. P.

Yadav and H. Y. Kim, *Int. J. Energy Res.*, 2023, **2023**, 1–46.

16   D. Acharya, A. Muthurasu, T. H. Ko, R. M. Bhattarai, T. Kim, S. H. Chae, S. Saidin, K. Chhetri and H. Y. Kim, *ACS Appl. Energy Mater.*, 2023, **6**, 9196–9206.

17   K. Kalinathan, D. P. DesRoches, X. Liu and P. G. Pickup, *J. Power Sources*, 2008, **181**, 182–185.

18   A. Le Comte, D. Chhin, A. Gagnon, R. Retoux, T. Brousse and D. Bélanger, *J. Mater. Chem. A*, 2015, **3**, 6146–6156.

19   G. Pognon, C. Cougnon, D. Mayilukila and D. Bélanger, *ACS Appl. Mater. Interfaces*, 2012, **4**, 3788–3796.

20   S. Legoupy, E. Lebègue and C. Cougnon, *Electrochem. commun.*, 2016, **70**, 47–50.

21   Ö. Taş, Z. Kudaş and D. Ekinci, *Diam. Relat. Mater.*, 2023, **138**, 110227.

22   A. Ejigu, I. A. Kinloch and R. A. W. Dryfe, *ACS Appl. Mater. Interfaces*, 2017, **9**, 710–721.